

Passive target localization using a geometric approach to the time-difference-of-arrival method

S. Wong
R. Jassemi-Zargani
D. Brookes
B. Kim
DRDC – Ottawa Research Centre

Defence Research and Development Canada

Scientific Report
DRDC-RDDC-2017-R079
June 2017

- © Her Majesty the Queen in Right of Canada, as represented by the Minister of National Defence, 2017
- © Sa Majesté la Reine (en droit du Canada), telle que représentée par le ministre de la Défense nationale, 2017

Abstract

Passive sensing offers a viable and effective means of detecting and geolocating small flying targets such as micro- and nano-drones by exploiting their radio-frequency signal emissions. Target location using the time-difference-of-arrival (TDOA) method is investigated. For target localization in three-dimensional space, a set of three non-linear TDOA equations is required. Each equation contains a TDOA measurement processed from signals detected by a pair of receivers. A system of four receivers is needed to generate three independent TDOA measurements. The solution to each TDOA equation is represented by a hyperboloid surface. The intersection of three hyperboloid surfaces is then computed to determine the target location. This geometric approach to solving the TDOA problem is taken in this study.

The target localization problem is analyzed by examining the effect of TDOA measurement errors on the localization accuracy. The errors are modelled by the Cramer-Rao Lower Bound estimate in processing the signals through a cross-correlator. Results indicate that the accuracy in three-dimensional target localization is dependent on not only the TDOA measurement errors, but also on the receiver system geometry. It is found that four receivers in a non-coplanar geometry configuration offer the best three-dimensional localization accuracy.

Localization of multiple targets is also investigated. Accurate localization results for up to ten moving targets have been obtained by applying the geometric approach. A discussion on how the geometric approach could be exploited for real-time multi-target localization is given. This will potentially offer a practical capability in defence and security applications.

Significance to defence and security

One of the future challenges in Intelligence, Surveillance and Reconnaissance (ISR) for the Canadian Armed Forces (CAF) is to monitor air activities in the Arctic. Awareness of foreign commercial and military activities will enable Canada to address potential threats to Arctic sovereignty. In particular, there have been increasing concerns on the use of drones by foreign entities for military surveillance purposes and natural resource prospecting by multi-national corporations. Strategic and sensitive areas are vulnerable to these types of intrusions and threaten Canada's national interests. As drones are becoming more affordable and more accessible, there will be more occurrences of multi-drone intrusion. A passive capability for detection and tracking multi-target activities will allow Canada to act on potential threats in a timely manner.

Furthermore, the advent of drone, sensor and data communication technologies will undoubtedly pose serious threats to the CAF's operations, especially those in the Arctic. It is foreseen that the CAF could be deploying an expeditionary force patrolling the Arctic in the future to maintain sovereignty; this could potentially bring them in contact with foreign state-armed or privately-armed forces. Mobile forward operating bases for the CAF and sensitive operating areas will be vulnerable to foreign drone ISR activities. It is imperative that the CAF is aware of any adversarial spying activities monitoring its operations; thus base protection and security will be of great concerns. A capability in countermeasures against drone surveillance will be necessary in

order to provide security and protection for the CAF, allowing them to conduct their operations effectively in the Arctic.

Passive sensing of drones can also provide security measures against covert surveillance of high-value infrastructure assets by rogue elements; these targets include Parliament Hill, National Defence Headquarters, and nuclear power plants. Concerns over drone-airplane collisions around airports and military air-fields can also be addressed by passive sensing of drones intruding into restricted airspace. In addition, drone operators on the ground near airports can be detected and located as well.

Résumé

Le captage passif offre un moyen viable et efficace de détecter et de géolocaliser de petites cibles volantes, par exemple des microdrones et des nanodrones, en exploitant leurs émissions de signaux en radiofréquence. La détermination de l'emplacement de la cible grâce à la méthode de la différence entre les temps d'arrivée (TDOA) est à l'étude. Pour localiser la cible dans un espace tridimensionnel, un ensemble de trois équations TDOA non linéaires est nécessaire. Chaque équation contient une mesure de TDOA traitée à partir des signaux détectés par une paire de récepteurs. Un système à quatre récepteurs est nécessaire pour générer trois mesures de TDOA indépendantes. La solution à chaque équation de TDOA est représentée par une surface hyperboloïde. L'intersection de trois surfaces hyperboloïdes est ensuite calculée afin de déterminer l'emplacement de la cible. C'est cette méthode géométrique qui est utilisée pour résoudre le problème de TDOA dans l'étude en question.

Le problème de repérage d'une cible est analysé en examinant l'effet des erreurs de mesure de TDOA sur l'exactitude du repérage. Les erreurs sont modélisées par l'estimation de la borne inférieure de Cramer-Rao pour le traitement des signaux par l'entremise d'un récepteur à corrélateur croisé. Les résultats indiquent que l'exactitude du repérage tridimensionnel d'une cible dépend non seulement des erreurs de mesure de TDOA, mais aussi de la géométrie du système de récepteur. On a déterminé qu'une configuration à quatre récepteurs disposés selon une géométrie non-coplanaire offrait la plus grande exactitude de repérage tridimensionnel.

Le repérage de cibles multiples est aussi à l'étude. Des résultats de repérage exacts pour jusqu'à dix cibles en mouvement ont été obtenus en appliquant la méthode géométrique. Un exposé est donné sur la façon dont la méthode géométrique pourrait être exploitée pour repérer des cibles multiples en temps réel. Cette méthode a le potentiel d'offrir des applications pratiques pour la défense et la sécurité.

Importance pour la défense et la sécurité

L'un des prochains enjeux en matière de renseignement, surveillance et reconnaissance (RSR) pour les Forces armées canadiennes (FAC) est de surveiller les activités aériennes dans l'Arctique. La vigilance relative aux activités commerciales et militaires étrangères permettra au Canada de répondre aux menaces potentielles à sa souveraineté dans l'Arctique. Plus particulièrement, l'utilisation de drones par des entités étrangères aux fins de surveillance militaire et par des corporations multinationales aux fins de prospection des ressources naturelles soulève des préoccupations croissantes. Des secteurs stratégiques et sensibles sont vulnérables à ces types d'intrusion, lesquels menacent les intérêts nationaux du Canada. Plus les drones deviendront abordables et accessibles, plus il y aura d'occurrences d'intrusion par des drones multiples. Une capacité de détection passive et de suivi des activités de cibles multiples permettra au Canada de répondre aux menaces potentielles en temps opportun.

Qui plus est, l'arrivée des technologies de drones, de capteurs et de communication par données posera indubitablement des menaces sérieuses aux opérations des FAC, plus particulièrement

celles qui se tiendront dans l'Arctique. Il est prévu dans l'avenir que les FAC pourraient déployer une force expéditionnaire afin de patrouiller dans l'Arctique pour y maintenir la souveraineté du Canada. Cette force pourrait entrer en contact avec les forces armées d'un état étranger ou des forces armées privées. Les bases d'opérations avancées mobiles des FAC et les secteurs d'opérations sensibles seront vulnérables aux activités de RSR de drones étrangers. Il est impératif que les FAC demeurent vigilantes face à toute activité d'espionnage de ses opérations par des intérêts étrangers; la protection et la sécurité des bases seront donc très préoccupantes. Il sera nécessaire d'établir une capacité de contremesures contre la surveillance par des drones afin d'assurer la sécurité et la protection des FAC et de leur permettre de mener avec efficacité leurs opérations dans l'Arctique.

Le captage passif des drones peut aussi offrir des mesures de sécurité contre la surveillance secrète d'infrastructures à valeur élevée par des éléments indésirables, par exemple la Colline du Parlement, les quartiers généraux de la Défense nationale ainsi que les centrales nucléaires. Le captage passif des drones qui pénètrent dans un espace aérien réglementé peut aussi servir à répondre aux préoccupations relatives aux collisions drones-avions près des aérodromes militaires et des aéroports. De plus, cette technologie permettra de détecter et de repérer les utilisateurs de drone au sol à proximité des aéroports.

Table of contents

Abstract	i
Significance to defence and security	i
Résumé	iii
Importance pour la défense et la sécurité	iii
Table of contents	v
List of figures	vii
List of tables	ix
1 Introduction	1
2 Target localization using TDOA method	3
2.1 TDOA for passive location	3
2.2 TDOA equations for determining target location	4
2.3 Geometric approach	4
2.4 Algebraic approach	8
3 TDOA measurements and errors	10
3.1 Mono-static radar ambiguity function	10
3.2 Generalized ambiguity function for passive sensing	11
3.3 TDOA measurement errors	18
3.3.1 TDOA measurement error modelling	20
3.3.2 Computing TDOA measurements with errors	21
4 Target location by intersection of hyperboloids	25
4.1 Locating target with coplanar receivers	25
4.1.1 Putting the hyperboloids in global coordinate frame	25
4.1.2 Error-free TDOA measurements as reference	27
4.1.3 Target localization from TDOA measurements with errors	29
4.2 Locating target with non-coplanar receivers	32
4.2.1 Non-coplanar receivers in the global coordinate frame	32
4.2.2 Non-coplanar target localization	34
4.3 Geometry-based target localization performance	35
5 Multi-target detection and tracking	38
5.1 A seven-target scenario case study	38
5.2 Multi-target localization	40
5.2.1 Target localization using coplanar receiver configuration	42
5.2.2 Effect of receiver-pair tilt in non-coplanar configuration	45
5.3 Overlapping TDOA measurements	46
5.3.1 Analysis of target localization with overlapping TDOA values	48
5.4 Approach to real-time multi-target processing	50
6 Conclusions	52

References	53
Annex A Frequency waveforms	57
List of symbols/abbreviations/acronyms/initialisms	61

List of figures

Figure 1:	Passive sensing system configuration; a) plan view, b) three-dimensional view.	3
Figure 2:	A pair of receivers (S1-S2) and a target are situated in a two-dimensional plane in the local coordinate frame.	5
Figure 3:	Hyperboloids in local coordinate frame (x',y',z') in three dimensions.	7
Figure 4:	A hyperboloid representing the TDOA of an air target as detected by a pair of receivers in local coordinate frame.	7
Figure 5:	A schematic of target signal detection by a pair of receivers.. . . .	12
Figure 6:	a) a range-difference profile signal without noise; b) with noise SNR = 12 dB.	20
Figure 7:	Superposition of twenty range-difference profile signals with noise, SNR = 12 dB.	20
Figure 8:	Three intersecting hyperboloids from three TDOA measurements.	28
Figure 9:	Intersection of three hyperbolic curves at a slice of target altitude, $z = 1000$ m.	29
Figure 10:	Comparison between computed target track (red diamonds) and ground truth (black circles). CRLB parametric values used: $\beta = 20$ MHz, $(S/N)_T = 12$ dB..	31
Figure 11:	A seven-target scenario with multiple flight paths depicted in the monitored area; target positions at different time instants are given by the black circles and the positions of receivers S1, S2, S3, S4 are indicated by the green squares.	38
Figure 12:	Cross-correlation outputs from a receiver-pair displaying seven detected target peaks as their corresponding TDOA measurement values along the range—difference axis.	39
Figure 13:	Computed target locations (x,y) from a non-coplanar configuration. S2: $Z_2 = 200$ m; CRLB parametric values used: $\beta = 20$ MHz, $(S/N)_T = 12$ dB..	41
Figure 14:	Computed target locations (x,y) from a non-coplanar configuration. S2: $Z_2 = 200$ m, CRLB parametric values used: $\beta = 20$ MHz, $(S/N)_T = 32$ dB..	42
Figure 15:	Computed target locations from a coplanar receiver configuration. S2: $Z_2 = 0$ m, CRLB parametric values used: $\beta = 20$ MHz, $(S/N)_T = 12$ dB..	43
Figure 16:	Computed target locations from a coplanar receiver configuration. S2: $Z_2 = 0$ m, CRLB parametric values used: $\beta = 20$ MHz, $(S/N)_T = 32$ dB..	44
Figure 17:	Computed target locations from a no-coplanar receiver configuration S2: $Z_2 = 400$ m, CRLB parametric values used: $\beta = 20$ MHz, $(S/N)_T = 12$ dB..	46
Figure 18:	Flight paths for a ten-target scenario; target positions at ten time instants are given by the small open circles.	47
Figure 19:	Computed target locations (x,y) from TDOA measurements with overlapping values. S2: $Z_2 = 200$ m (non-coplanar), CRLB parametric values used: $\beta = 20$ MHz, $(S/N)_T = 32$ dB.	49

Figure A.1:	Schematic of the stepped-frequency waveform.	58
Figure A.2:	Schematic of the chirp pulse-compression waveform.	60
Figure A.3:	Schematic of the frequency-modulated continuous waveform.	60

List of tables

Table 1:	TDOA measurement values with no errors..	22
Table 2:	Cramer-Rao Lower Bound rms error ϵ for different signal bandwidth values.	22
Table 3:	TDOA measurements for signal with $\beta = 1$ MHz and $(S/N)_T = 12$ dB.	23
Table 4:	TDOA measurements for signal with $\beta = 20$ MHz and $(S/N)_T = 12$ dB.	23
Table 5:	TDOA measurements for signal with $\beta = 300$ MHz and $(S/N)_T = 12$ dB.	24
Table 6:	Ground-truth locations of receivers in global coordinates.	25
Table 7:	Receivers S1 and S2 locations in local coordinate frame.	26
Table 8:	Comparisons of target localization from error-free TDOA measurements and target ground-truth positions for coplanar receiver system.	28
Table 9:	Comparisons of target localization from TDOA measurements with errors and actual target positions for coplanar receiver system. CRLB parametric values used: $\beta = 1$ MHz and $(S/N)_T = 12$ dB.	29
Table 10:	Comparisons of target localization from TDOA measurements with errors and actual target positions for coplanar receiver system. CRLB parametric values used: $\beta = 20$ MHz and $(S/N)_T = 12$ dB.	30
Table 11:	Comparisons of target localization from TDOA measurements with errors and actual target positions for coplanar receiver system. CRLB parametric values used: $\beta = 300$ MHz and $(S/N)_T = 12$ dB.	30
Table 12:	Comparisons of target localization from TDOA measurements with errors and actual target positions for non-coplanar receiver system. S2: $Z_2 = 200$ m, CRLB parametric values used: $\beta = 1$ MHz, $(S/N)_T = 12$ dB.	35
Table 13:	Comparisons of target localization from TDOA measurements with errors and actual target positions for non-coplanar receiver system. S2: $Z_2 = 200$ m, CRLB parametric values used: $\beta = 20$ MHz, $(S/N)_T = 12$ dB.	36
Table 14:	Comparisons of target localization from TDOA measurements with errors and actual target positions for non-coplanar receiver system. S2: $Z_2 = 200$ m, CRLB parametric values used: $\beta = 300$ MHz, $(S/N)_T = 12$ dB.	36
Table 15:	Comparisons of target localization from TDOA measurements with errors and actual target positions for non-coplanar receiver system. S2: $Z_2 = 500$ m, CRLB parametric values used: $\beta = 1$ MHz, $(S/N)_T = 12$ dB.	37
Table 16:	A permutation of all possible combinations of the TDOA values for a 2-target scenario.. . . .	40
Table 17:	Computed target altitudes from a non-coplanar configuration. S2: $Z_2 = 200$ m. CRLB parametric values used: $\beta = 20$ MHz, $(S/N)_T = 12$ dB. Actual target altitude = 1000 m.	41

Table 18:	Computed target altitudes from a non-coplanar receiver configuration. S2: $Z_2 = 200$ m, CRLB parametric values used: $\beta = 20$ MHz, $(S/N)_T = 32$ dB. Actual target altitude = 1000 m.	42
Table 19:	Computed target altitudes from a coplanar configuration. S2: $Z_2 = 0$ m, CRLB parametric values used: $\beta = 20$ MHz, $(S/N)_T = 12$ dB. Actual target altitude = 1000 m.	43
Table 20:	Computed target altitudes from a coplanar receiver configuration. S2: $Z_2 = 0$ m, CRLB parametric values used: $\beta = 20$ MHz, $(S/N)_T = 32$ dB. Actual target altitude = 1000 m.	45
Table 21:	Computed target altitudes from a non-coplanar receiver configuration. S2: $Z_2 = 400$ m, CRLB parametric values used: $\beta = 20$ MHz, $(S/N)_T = 12$ dB. Actual target altitude = 1000 m.	46
Table 22:	Occurrence of overlapping TDOA measurements in a ten-target scenario, resulted in only nine TDOA values at time instant t. S2: $Z_2 = 200$ m, CRLB parametric values used: $\beta = 20$ MHz, $(S/N)_T = 32$ dB.	47
Table 23:	TDOA measurement values of individual targets and overlapped TDOA measurement values between two targets. S2: $Z_2 = 200$ m, CRLB parametric values used: $\beta = 20$ MHz, $(S/N)_T = 32$ dB.	48
Table 24:	Target altitudes computed from TDOA measurements with overlapped values. Actual target altitude = 1000 m.	49
Table 25:	Computation time consumed in target localization processing for different number of targets detected using sequential processing.	51

1 Introduction

Mini-drones and micro-drones are seen as technologies that are increasingly posing serious threats to military operations, public security, and national interests. These threats include military scouting and targeting reconnaissance by adversaries, potential drone-airplane collisions near airport/airfield runways, security breaches around nuclear power plants, intrusions to sensitive government infrastructures, and natural resources prospecting in the Arctic by private multi-national corporations. A proliferation of these flying machines is expected to inundate the airspace in the not too distant future; thus a capability to detect and track these targets is foreseen to be a useful asset and will be in demands in the defence and security domains.

Detecting small drone targets can be quite challenging for conventional methods such as active-radar or EO/IR sensing because of their small size, their construction materials and low-thermal emission characteristics. On the other hand, passive detection methods can be quite useful for detecting small drones. For example, radio-frequency (RF) emissions from drones such as First-Person-View remote piloting, image data transmissions and telemetry communication can be exploited for passive detection and tracking.

Passive target detection and localization methods are widely used in many applications, for example, navigation, search and rescue, surveillance, and electronic warfare. These have been areas of active research for over the past many decades. A well-established method used in passive target location of non-cooperative targets exploiting the target's own RF emissions is the time-difference-of-arrival (TDOA) measurement technique [1,2]. It deploys a number of time-synchronized sensors to produce a fix on the target's location.

TDOA methods have been researched and developed extensively. The majority of the TDOA signal processing algorithms reported in the literature are based on the algebraic approach in solving a set of three non-linear hyperbolic equations with three unknowns [3,4,5]. Essentially, these equations are solved by numerical iterative methods to locate a target. There are a number of variations on the techniques developed for the algebraic approach, iterative statistical methods [2,5,6,7] and closed-form algebraic solutions [3,8,9,10]. However, when the TDOA measurements from the sensors have sizable errors, the closed-form algebraic solution will have notable errors as a result, meaning poor target localization accuracy. Iterative techniques must then be applied to optimize the solution. Iterative numerical processing can be computationally intensive; thus it is a challenge to apply it to real-time applications.

As drones are becoming more affordable and more easily accessible, future target detection system will likely require a multi-target localization capability. In many of the applications, multi-target detection and real-time response are highly desirable. There are some reported works in the literature on multi-target localization; see for example [6,7,11]. They are analyzed via iterative numerical methods which are computational intensive; multi-target processing will demand even greater computing capacity. Furthermore, issues of consistency in iterative convergence are more complicated dealing with multi-target, requiring more complex algorithmic computations. Thus, the feasibility of real-time multi-target localization deploying iterative numerical methods becomes questionable.

An alternative approach to solving the TDOA problem is exploring the geometric approach in solving the set of nonlinear hyperbolic equations. This is equivalent to finding the intersection of three hyperboloids as the target location. There have been a number of investigations on the geometric approach [4,10,12,13]. In fact, a geometry-based solution had already been applied to the LOnG RAnge Navigation (LORAN) navigation system since the 1950s. A set of charts of hyperbolic lines of position in two dimensions was used as overlay to find the intersection as the location of the target. Although the operation of the LORAN system was shown to be successful, the mathematical solutions using geometry were considered as cumbersome because graphical charts had to be made and were used manually as overlays to find the target location [14].

Finding the intersection of a set of three hyperboloids geometrically in three dimensions to pinpoint target location fixes may be seen as a cumbersome and complex task. One of the purposes of this report is to show that a simple numerical procedure can be used to determine the intersecting location of the hyperboloids, and target location can be determined accurately. This can be done efficiently, and hence can offer a real-time processing capability.

A technical framework of the TDOA method and procedures based on the geometric approach for finding target locations will be examined and discussed in this report. It will be shown that multi-target localization can be obtained accurately in a relatively simple manner. Another reason in pursuing the geometric approach is that the hyperboloids can be pre-computed for a set of possible TDOA measured values for a given detection system configuration, and look-up tables for the hyperboloids can then be compiled. With the advent of super-efficient search algorithms for accessing data files, large data storage capacity, and parallel computing, the problem of real-time multiple targets localization may be realized using look-up tables.

The objective of this report is to obtain a greater understanding on the technical aspects of passive target detection and localization based on RF signal emission from targets. The results can be used to address how a capability can be developed to detect and monitor the presence of multiple targets. A better understanding of the passive detection process will facilitate further development of practical solutions to deal with these new emerging threats.

2 Target localization using TDOA method

2.1 TDOA for passive location

Passive location of an emitting target using the TDOA method has been described and analyzed extensively in the literature for more than four decades [13]. The TDOA method is based on the principle of locating a target along a three-dimensional surface where the time difference of arrival of a target signal between a pair of synchronized receivers is constant. This surface is described by a hyperboloid. Using a group of four receivers stationed at different locations, three independent TDOA measurements can be made [3]. The TDOA measurements are then converted to hyperboloid surfaces. The intersecting point formed by the three hyperboloids determines the target's location in three-dimensional space.

In order to provide a clear illustration of how TDOA measurements can be made, a typical ground receiver configuration is used for illustration; this is shown in Figure 1. There are four receivers (S1, S2, S3, S4) in a passive detection unit. The receiver system in Figure 1 is configured in a “forward looking” mode; that is, the receivers are monitoring the airspace at the top of Figure 1a (yellow shaded area.) Also, the receivers are assumed to have a wide field of view in azimuth and elevation so that all four receivers monitor the same volume of airspace at the same time in staring-mode. The receiver locations are described in three dimensions by global coordinates, (x,y,z) , giving the passive system a three-dimensional geometry. The dimensions of the area of interest monitored by the system shown in Figure 1 correspond to area coverage in a typical small drone detection scenario where a drone typically emits 500 mW (EIRP) from its First Person View transmitter for remote piloting control.

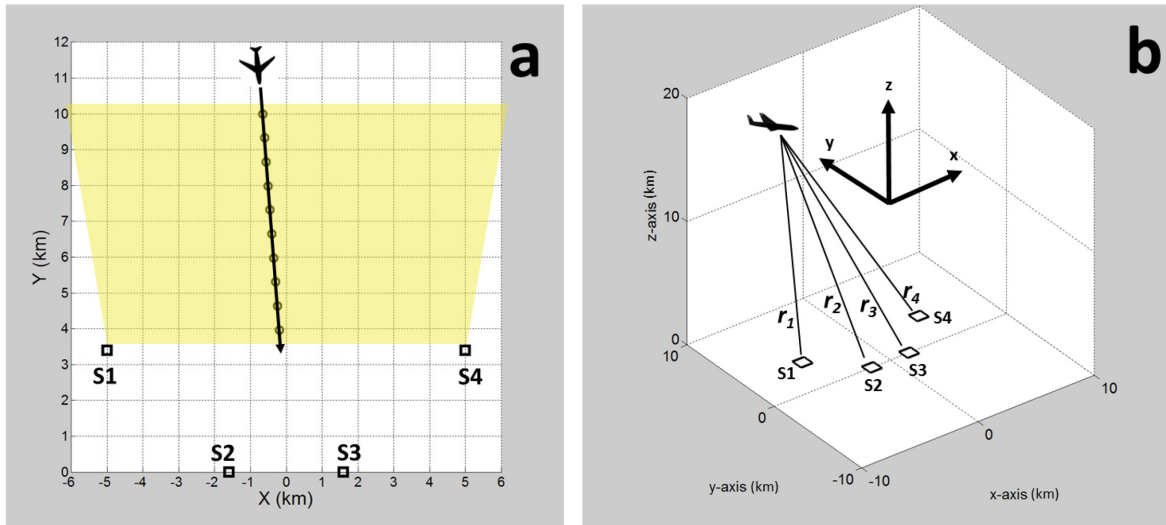


Figure 1: Passive sensing system configuration; a) plan view, b) three-dimensional view.

2.2 TDOA equations for determining target location

Three time-synchronized coherent receiver-pairs, S1-S2, S3-S4 and S1-S4 are formed from a group of four receivers in Figure 1 to collect three independent sets of TDOA measurement data. For example, TDOA τ_{12} is measured by the receiver-pair S1-S2, TDOA τ_{34} by the receiver-pair S3-S4 and TDOA τ_{14} is measured by the receiver-pair S1-S4. Time synchronization between receivers can be achieved readily using GPS-disciplined oscillators. Details on how the TDOA measurements are made will be given later in Section 3. It is sufficient to say for now that three independent TDOA measurements are needed to locate a target. The set of three TDOA equations are,

$$\begin{aligned} d_{12} &= c\tau_{12} = r_1 - r_2 \\ d_{34} &= c\tau_{34} = r_3 - r_4 \\ d_{14} &= c\tau_{14} = r_1 - r_4 \end{aligned} \tag{1}$$

where $d_{ij} = c\tau_{ij}$ is the range-difference (i.e., TDOA measurements expressed in length unit) of the target relative to receiver i and receiver j , c is the speed of light, and $r_i = ((x - X_i)^2 + (y - Y_i)^2 + (z - Z_i)^2)^{1/2}$ is the L_2 -norm (Euclidean) distance between the target (x, y, z) and receiver (X_i, Y_i, Z_i) (see Figure 1b), and $i, j = 1, 2, 3, 4$. For simplicity and consistency, d_{ij} will be referred to as the “TDOA measurement.” Each of the equations in Equation (1) represents a three-dimensional hyperboloid surface geometrically; this will be discussed in more details in Section 2.3. Since the receiver positions (X_i, Y_i, Z_i) are known and the TDOA measurement values d_{ij} can be made, Equation (1) with three independent equations can hence be solved for the three unknown target location coordinates (x, y, z) to find the target location.

There are two distinct approaches to solving the TDOA equations in Equation (1): a geometric approach, and an algebraic approach. Both approaches will be described in the following subsections of this chapter. In this report, the analysis of target localization will be conducted using the geometric approach. This approach offers a simpler algorithm for multi-target localization, and has the potential for real-time processing.

2.3 Geometric approach

This approach is a geometry-based method to generate three hyperboloids from the three equations in Equation (1), and then looks for the intersecting point among the three hyperboloids as the target location. Geometrically, Equation (1) describes three intersecting hyperbolic surfaces. It will be shown that in the ideal case when there is no TDOA measurement error in the d_{ij} , the three hyperboloids do intersect at a point; this will be presented in the analysis in Section 4. However in practice, the TDOA measurements will always contain errors due to system noise and target signal characteristics such as bandwidth; only an estimate of the target location can be made. The localization accuracy is thus subject to the size of the TDOA measurement error.

Mathematically, the geometric form of each hyperboloid in Equation (1) can be more simply described by considering each pair of receivers in its own local coordinate frame of reference.

This is to distinguish it from the common coordinate frame in which all the receivers and targets must reside in order to determine the target location; this common frame shall be called the global coordinate frame.

Receiver-pair S1-S2 will be used as an illustrative example. In the local frame, the receiver-pair separated by a distance d is placed on the x' -axis symmetrically. That is to say, receiver S1 has the coordinate $(X', Y', Z')_1 = (-d/2, 0, 0)$, and receiver S2 has the coordinate $(X', Y', Z')_2 = (d/2, 0, 0)$. Furthermore, the y' axis is oriented such that the target is situated in the x' - y' plane; i.e., with coordinates $(x', y', 0)$. Thus, a local frame is defined in which the two receivers and the target are all confined in a two-dimensional plane (i.e., x' - y' plane). This is illustrated schematically in Figure 2.

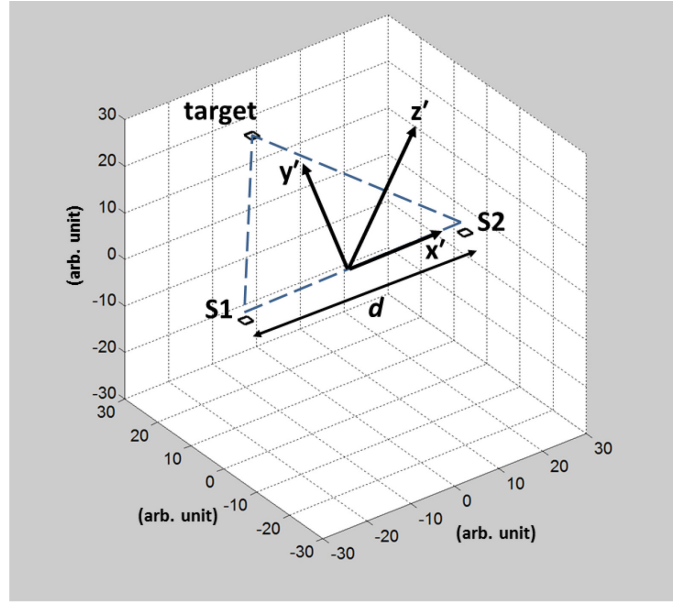


Figure 2: A pair of receivers (S1-S2) and a target are situated in a two-dimensional plane in the local coordinate frame.

Using the first equation in Equation (1) for the S1-S2 receiver-pair, and substituting in the receivers and target coordinates,

$$\begin{aligned}
 d_{12} &= r_1 - r_2 \\
 &= \sqrt{(x' - X_1')^2 + (y' - Y_1')^2} - \sqrt{(x' - X_2')^2 + (y' - Y_2')^2} \\
 &= \sqrt{\left(x' + \frac{d}{2}\right)^2 + y'^2} - \sqrt{\left(x' - \frac{d}{2}\right)^2 + y'^2}
 \end{aligned} \tag{2}$$

After some algebraic rearrangements, Equation (2) can be re-expressed as,

$$\frac{x'^2}{\left(\frac{d_{12}^2}{4}\right)} - \frac{y'^2}{\left(\frac{d^2}{4} - \frac{d_{12}^2}{4}\right)} = 1 \quad (3)$$

Equation (3) is a “hyperbola of two-sheet” in two dimensions [15]. A three-dimensional hyperboloid can be generated by the method of volume of revolution about the x' -axis. The hyperboloid is thus given by,

$$\frac{x'^2}{a^2} - \left(\frac{y'^2}{b^2} + \frac{z'^2}{b^2}\right) = 1 \quad (4)$$

where $a = (d_{12}/2)$, $b = (d^2 - d_{12}^2)^{1/2}/2$, $d > d_{12}$. Physically, the hyperboloid surface represents an isochrone where a point anywhere on the surface has the same TDOA with respect to receivers S1 and S2. Recasting Equation (4) in the form,

$$x' = \pm |a| \left(1 + \left(\frac{y'^2}{b^2} + \frac{z'^2}{b^2}\right)\right)^{1/2} \quad (5)$$

It can be seen that there are two distinct hyperboloid surfaces that can exist; one has $+|a|$ value and the other has $-|a|$ value in Equation (5). These two hyperboloids are shown in Figure 3. Moreover, because the hyperboloid is a surface generated from volume of revolution about the x' -axis, it is therefore symmetrical azimuthally in a rotation about the x' -axis. Thus, the local frame axes can be redefined, with the z' -axis as pointing vertically upward as illustrated in Figure 3.

Recall from Equation (4) that the parameter a , is effectively the TDOA measurement value d_{12} . The TDOA measurement value can take on either positive or negative value; this can be clearly seen from Equation (2). If the target is closer to receiver S2 than to receiver S1, then a is positive because $d_{12} = r_1 - r_2$ is positive; otherwise, a is negative. When the target is exactly the same distance from both receivers (i.e., $a = 0$), Equation (5) degenerates into a plane described by $x' = 0$.

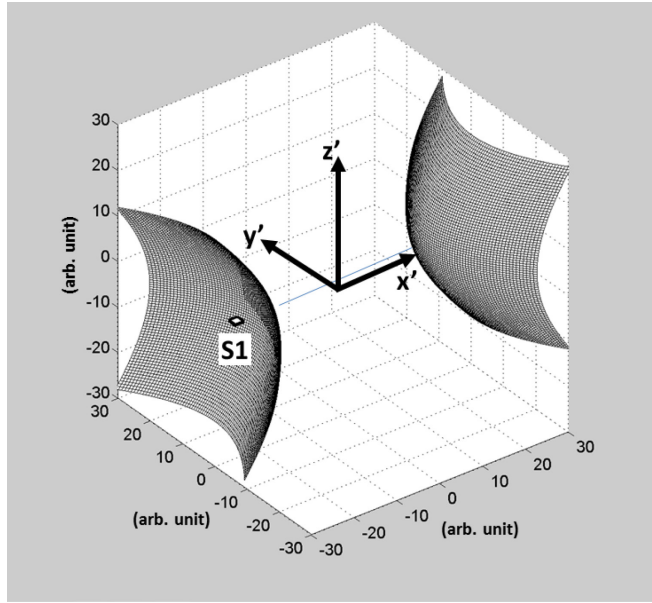


Figure 3: Hyperboloids in local coordinate frame (x', y', z') in three dimensions.

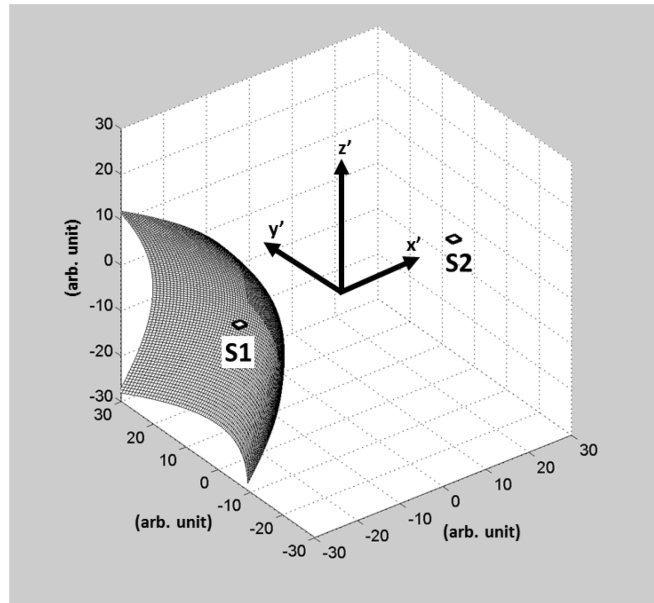


Figure 4: A hyperboloid representing the TDOA of an air target as detected by a pair of receivers in local coordinate frame.

The TDOA measurement d_{12} of a target will have either a plus or minus sign associated with it. Therefore, only one of the two hyperboloids in Figure 3 is valid. If the TDOA measurement value d_{12} is negative (i.e., $r_1 < r_2$), only the hyperboloid closer to receiver S1 is valid; this is shown in Figure 4. Thus the geometric solution automatically constrains the solution to the correct sector of

the airspace volume. In effect, the hyperboloid surface shown in Figure 4 represents the solution to the first TDOA equation in Equation (1).

Hyperboloids for receiver-pairs S3-S4 and S1-S4 can be obtained in the exact same manner in their own local coordinate frame (x',y',z') . The three hyperboloids will then be relocated to the common global coordinate frame (x,y,z) and properly oriented relative to their respective receiver-pairs so that the intersection of the three hyperboloid can be determined. The process of locating the target from three intersecting hyperboloids will be discussed in more details in Section 4.

2.4 Algebraic approach

The set of nonlinear TDOA equations in Equation (1) can also be solved by numerical iterative methods such as Least Squares, Taylor series, and other optimization techniques [16,17,18]. But they are computationally intensive and could have convergence issues that require further complex algorithmic attention; hence they are not likely to offer real-time computing. A closed form algebraic solution to the set of TDOA equations given by Equation (1) exists [3,16]. The closed form solution offers an elegant and efficient (low computational demand) means of handling the TDOA equations. It is frequently applied in TDOA analysis in the literature [5,8,9,19,20]. Using a receiver system with five receivers as an example, the closed form solution is obtained as follows. First, the distance from the i -th receiver to the target in Equation (1) can be written as,

$$r_i = \sqrt{(x - X_i)^2 + (y - Y_i)^2 + (z - Z_i)^2}, \quad (6)$$

where the receiver index $i=1,2,3,4,5$ and (x,y,z) are the coordinates of the unknown target's location. Rewriting Equation (1) as,

$$r_i^2 = (d_{ij} + r_j)^2 \quad (7)$$

And substituting r_i and r_j as given by Equation (6), Equation (7) can be re-expressed algebraically as,

$$d_{ij} \|\mathbf{R}_j - \mathbf{R}\| + (\mathbf{R}_i - \mathbf{R}_j) \cdot \mathbf{R} = \frac{1}{2}(\|\mathbf{R}_i\|^2 - \|\mathbf{R}_j\|^2 - d_{ij}^2) \quad (8)$$

where $\mathbf{R}_i = (X_i, Y_i, Z_i)$, $\mathbf{R}_j = (X_j, Y_j, Z_j)$, $\mathbf{R} = (x, y, z)$, $\|\mathbf{R}_i\| = (X_i^2 + Y_i^2 + Z_i^2)^{1/2}$, $\|\mathbf{R}_j\| = (X_j^2 + Y_j^2 + Z_j^2)^{1/2}$, and $\|\mathbf{R}_j - \mathbf{R}\| = ((X_j - x)^2 + (Y_j - y)^2 + (Z_j - z)^2)^{1/2}$ is the L_2 -norm distance from the target to the j -th receiver. Next, assigning receiver subscript $j=1$ as the reference receiver of the system such that the TDOA measurements of the other receivers are made relative to receiver S1 (i.e., d_{i1} , $i = 2,3,4,5$), Equation (8) can then be written in matrix form as,

$$\begin{bmatrix} d_{21} & X_2 - X_1 & Y_2 - Y_1 & Z_2 - Z_1 \\ d_{31} & X_3 - X_1 & Y_3 - Y_1 & Z_3 - Z_1 \\ d_{41} & X_4 - X_1 & Y_4 - Y_1 & Z_4 - Z_1 \\ d_{51} & X_5 - X_1 & Y_5 - Y_1 & Z_5 - Z_1 \end{bmatrix} \begin{bmatrix} \|\mathbf{R}_1 - \mathbf{R}\| \\ x \\ y \\ z \end{bmatrix} = \frac{1}{2} \begin{bmatrix} \|\mathbf{R}_2\|^2 - \|\mathbf{R}_1\|^2 - d_{21}^2 \\ \|\mathbf{R}_3\|^2 - \|\mathbf{R}_1\|^2 - d_{31}^2 \\ \|\mathbf{R}_4\|^2 - \|\mathbf{R}_1\|^2 - d_{41}^2 \\ \|\mathbf{R}_5\|^2 - \|\mathbf{R}_1\|^2 - d_{51}^2 \end{bmatrix} \quad (9)$$

where $\|\mathbf{R}_l - \mathbf{R}\|$ is an unknown distance between the target at (x,y,z) and the reference receiver at \mathbf{R}_l . $\|\mathbf{R}_l - \mathbf{R}\|$ is considered as an independent variable. The closed form method requires $(K-1)$ TDOA measurements d_{il} , where K is the number of receivers in the system. Thus, with $K = 5$ receivers, there are four equations and four unknowns; hence $(\|\mathbf{R}_l - \mathbf{R}\|, x, y, z)$ can be solved explicitly. It should be noted that the minimal number of receivers required to generate a three-dimensional solution is $K = 4$. With four receivers and consider only three unknown variables, Equation (9) can be rewritten as,

$$\begin{bmatrix} d_{21} & X_2 - X_1 & Y_2 - Y_1 \\ d_{31} & X_3 - X_1 & Y_3 - Y_1 \\ d_{41} & X_4 - X_1 & Y_4 - Y_1 \end{bmatrix} \begin{bmatrix} \|\mathbf{R}_1 - \mathbf{R}\| \\ x \\ y \end{bmatrix} = \frac{1}{2} \begin{bmatrix} \|\mathbf{R}_2\|^2 - \|\mathbf{R}_1\|^2 - d_{21}^2 \\ \|\mathbf{R}_3\|^2 - \|\mathbf{R}_1\|^2 - d_{31}^2 \\ \|\mathbf{R}_4\|^2 - \|\mathbf{R}_1\|^2 - d_{41}^2 \end{bmatrix} \quad (10)$$

There are $(K-1) = 3$ equations and three unknowns; $\|\mathbf{R}_l - \mathbf{R}\|, x, y$ can be solved. Since $\|\mathbf{R}_l - \mathbf{R}\| = ((X_l - x)^2 + (Y_l - y)^2 + (Z_l - z)^2)^{1/2}$, z can therefore be computed as a quadratic solution of $\|\mathbf{R}_l - \mathbf{R}\|$. This is known as the minimally determined problem.

For the closed form solution described above, the set of nonlinear TDOA equations of Equation (1) has been transformed into a set of linear equation (Equation (10)) with three independent unknown variables; that is, $\|\mathbf{R}_l - \mathbf{R}\|$ is assumed to be independent of x and y . It has been shown that the solutions from the linearized equations are equivalent to those of the original nonlinear equations only when the TDOA measurement errors in the d_{il} approaches zero [8,16]. Thus, accurate target location (x,y,z) output is attainable in closed form only if the errors in d_{il} are small.

In most real-world cases, the errors in the TDOA measurements d_{il} may not be small. In fact, they can be quite large in some practical cases; this will be discussed in Section 3. Therefore, it would compound the inaccuracy in the closed form solution. Iterative methods will still be required in order to obtain better accuracy in estimating target location; the closed form solution may provide useful initial values to speed up the iterative convergence process. In practical applications where errors in the TDOA measurements can be large, the closed form solution may not be very useful.

3 TDOA measurements and errors

TDOA measurements (d_{ij}) are obtained after the signals, detected by a pair of time-synchronized passive receivers, are processed through a cross-correlator [21,22,23]. A detailed description of the cross-correlation process for obtaining the TDOA measurement d_{ij} from a radar signal processing perspective will be given in this section. It is well known that the accuracy of target localization is subject to measurement error in d_{ij} [1,3,8,12]. The amount of error introduced can be estimated using the Cramer-Rao Lower Bound (CRLB) [24,25]. The analysis of TDOA measurements with errors will also be discussed in this section. Using examples of different passive detection scenarios, the size of TDOA measurement error and its effect on the target localization accuracy will be characterized in Section 4.

3.1 Mono-static radar ambiguity function

In order to see how TDOA measurements are processed, the conventional radar signal analysis is used as a model. To establish a parallel between passive signal processing and radar signal processing, a brief overview of the conventional radar signal analysis using the radar ambiguity function is first given to introduce some of the basic parameters that are relevant to the TDOA problem.

For conventional active mono-static radar signal processing, the ambiguity function is given by [26],

$$\chi(\tau_d, v_D) = \int s_1(t) s_1^*(t - \tau_d) \exp(j2\pi v_D t) dt \quad (11)$$

The first factor $s_1(t)$ is the reference signal originated from the radar transmitter, and is assumed to be at rest in a relative reference frame with respect to its surrounding. The second factor $s_1(t - \tau_d) \exp(j2\pi v_D t)$ is the detected echo bouncing off a moving target at a distance R from the radar, and the target possesses a line-of-sight Doppler frequency v_D as seen by the radar. The radar ambiguity function is essentially a cross-correlation process between the transmitted radar signal and the detected echo scattered back from a target. The parameters τ_d and v_D are given by,

$$\begin{aligned} \tau_d &= \frac{2R}{c} \\ v_D &= \frac{2fv}{c} \end{aligned} \quad (12)$$

where τ_d is the two-way time delay of the transmitted pulse detected as echo by the radar receiver; c is the speed of light. The variable v_D is the Doppler frequency seen by the radar receiver; f is the radar carrier frequency and v is the line-of-sight velocity of the moving target relative to the radar. It should be noted that the ambiguity function χ is a function of the time delay τ_d and the Doppler frequency v_D . From these two variables, target range and target line-of-sight velocity can be determined.

3.2 Generalized ambiguity function for passive sensing

A similar expression can be written for passive signal detection employing two time-synchronized receivers. Consider a general scenario where two receivers and a RF emitting target are all in motion; this is depicted in Figure 5. The signal detected by receiver S1 at time t can be written as [27],

$$\begin{aligned} s_1(t) &= a_1(t) \exp(-j2\pi f t) \exp(j2\pi f \frac{R_{1T}(t)}{c}) \\ &= a_1(t) \exp(-j2\pi f (t - \tau_1')) \end{aligned} \quad (13)$$

where $a_1(t)$ is the temporal amplitude of the signal, f is the carrier frequency of the signal, and τ_1' , the time delay for the emitting signal from the target to reach receiver S1

$$\tau_1' = \frac{R_{1T}(t)}{c} \approx \frac{1}{c} (R_{1,0} - |(\mathbf{v}_1 - \mathbf{v}_T)|_{LOS} t) \quad (14)$$

is obtained by expanding the time-varying range $R_{1T}(t) = \|\mathbf{R}_1(t) - \mathbf{R}_T(t)\|$ using a first-order Taylor series. $R_{1,0} = R_{1T}(0)$ is the distance between the target and receiver S1 at time $t = 0$, i.e., at the beginning of the data collect of $s_1(t)$. $\mathbf{R}_1(t)$ and $\mathbf{R}_T(t)$ are the positional vectors for receiver S1 and the target; \mathbf{v}_1 and \mathbf{v}_T are the instantaneous velocity vectors at the time of signal sampling as shown in Figure 5. The line-of-sight (LOS) resultant of $(\mathbf{v}_1 - \mathbf{v}_T)$ provides a relative Doppler frequency of the target as seen by receiver S1. Substituting Equation (14) into Equation (13), $s_1(t)$ can be rewritten as,

$$\begin{aligned} s_1(t) &= a_1(t) \exp(-j2\pi f t) \exp(j2\pi f \frac{R_{1,0}}{c}) \exp(-j2\pi f \frac{|(\mathbf{v}_1 - \mathbf{v}_T)|_{LOS} t}{c}) \\ &= a_1(t) \exp(-j2\pi f (t - \frac{R_{1,0}}{c})) \exp(-j2\pi f \frac{|(\mathbf{v}_1 - \mathbf{v}_T)|_{LOS} t}{c}) \\ &= \mu_1(t - \tau_1) \exp(-j2\pi f_{D,1} t) \end{aligned} \quad (15)$$

where

$$\begin{aligned} \tau_1 &= \frac{R_{1,0}}{c} \\ f_{D,1} &= \frac{f}{c} |(\mathbf{v}_1 - \mathbf{v}_T)|_{LOS} \end{aligned} \quad (16)$$

Note that in Equation (15), the time delay τ_1 due to the target-to-receiver distance and the relative Doppler of the target $f_{D,1}$ as seen by the receiver are separated and grouped in two different

entities. The time delay is incorporated in the variable μ_1 ; the Doppler effect is expressed as a separate phase factor.

Similarly at receiver S2, the signal detected is given as,

$$\begin{aligned}
 s_2(t) &= a_2(t) \exp(-j2\pi f t) \exp(j2\pi f \frac{R_{2,0}}{c}) \exp(-j2\pi f \frac{|(\mathbf{v}_2 - \mathbf{v}_T)|_{LOS}}{c} t) \\
 &= a_2(t) \exp(-j2\pi f (t - \frac{R_{2,0}}{c})) \exp(-j2\pi f \frac{|(\mathbf{v}_2 - \mathbf{v}_T)|_{LOS}}{c} t) \\
 &= \mu_2(t - \tau_2) \exp(-j2\pi f_{D,2} t)
 \end{aligned} \tag{17}$$

where

$$\begin{aligned}
 \tau_2 &= \frac{R_{2,0}}{c} \\
 f_{D,2} &= \frac{f}{c} |(\mathbf{v}_2 - \mathbf{v}_T)|_{LOS}
 \end{aligned} \tag{18}$$

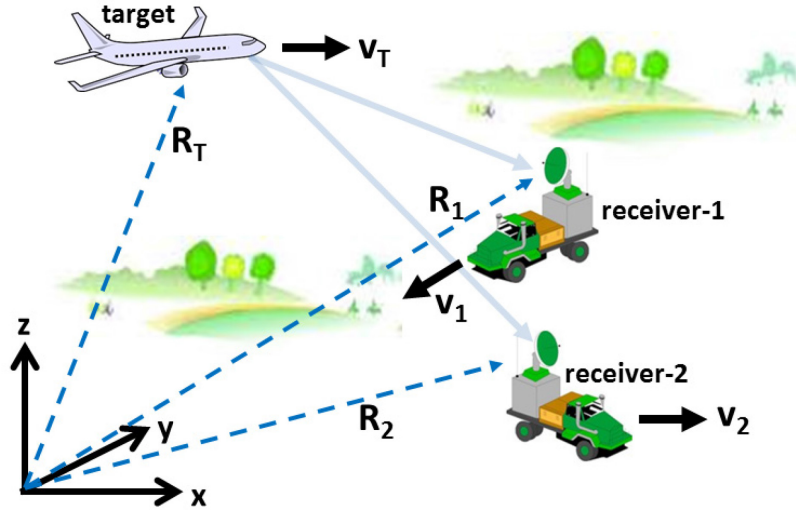


Figure 5: A schematic of target signal detection by a pair of receivers.

From Equation (15) and Equation (17), a generalized cross-ambiguity function can be defined as [28],

$$\begin{aligned}
 \chi(\tau_1, \tau_2, f_{D,1}, f_{D,2}) &= \int \mu_1(t - \tau_1) \mu_2^*(t - \tau_2) \exp(j2\pi(f_{D,2} - f_{D,1})t) dt \\
 &= \int a_1(t) \exp(-j2\pi f t) a_2(t) \exp(j2\pi f (t - (\tau_2 - \tau_1))) \exp(j2\pi(f_{D,2} - f_{D,1})t) dt
 \end{aligned} \tag{19}$$

by introducing a change of variable $t_0 = t - \tau_1$, and re-defining the variable t_0 as t . Furthermore, let

$$\begin{aligned}\tau &= \tau_2 - \tau_1 = \frac{(R_{2,0} - R_{1,0})}{c} \\ f_D &= f_{D,2} - f_{D,1} = \frac{f}{c} [|(\mathbf{v}_2 - \mathbf{v}_T)|_{LOS} - |(\mathbf{v}_1 - \mathbf{v}_T)|_{LOS}]\end{aligned}\tag{20}$$

and

$$\begin{aligned}\mu_1(t) &= a_1(t) \exp(-j2\pi f t) \\ \mu_2^*(t - \tau) &= a_2(t) \exp(j2\pi f (t - \tau))\end{aligned}\tag{21}$$

Equation (19) can be re-expressed as

$$\chi(\tau, f_D) = \int \mu_1(t) \mu_2^*(t - \tau) \exp(j2\pi f_D t) dt ,\tag{22}$$

arriving at the conventional form of the ambiguity function as given by Equation (11). There is a fundamental difference between Equations (11) and (22). The variables τ and f_D in Equation (22) are now taking on a different physical interpretation in the generalized cross-ambiguity function. From the forms of the variables given in Equation (20), τ describes the time-difference-of-arrival (TDOA) and f_D describes the frequency-difference-of-arrival (FDOA) of the target signal relative to the two receivers. What this means is that the target's position, given with respect to the two receivers, is a function of the TDOA and FDOA values.

In order to proceed to practical passive sensing processing, the cross-ambiguity function given in Equation (19) can be re-defined by introducing a pair of variables for the signals captured by each of the two receivers; i.e., rewriting Equations (15) and (17) as,

$$\begin{aligned}
\eta_1(t - \tau_1') &= a_1(t) \exp(-j2\pi ft) \exp(j2\pi f \frac{R_{1,0}}{c}) \exp(-j2\pi f_{D,1} t) \\
&= a_1(t) \exp(-j2\pi ft) \exp(j2\pi f \frac{1}{c} (R_{1,0} - |(\mathbf{v}_1 - \mathbf{v}_T)|_{LOS} t)) \\
&= a_1(t) \exp(-j2\pi f(t - \frac{R_{1,0}}{c} + \frac{1}{c} |(\mathbf{v}_1 - \mathbf{v}_T)|_{LOS} t)) \\
&= a_1(t) \exp(-j2\pi f(t - (\frac{R_{1,0}}{c} - \frac{1}{c} |(\mathbf{v}_1 - \mathbf{v}_T)|_{LOS} t))) \\
&= a_1(t) \exp(-j2\pi f(t - (\tau_1 - \frac{f_{D,1}}{f} t))) \\
&= a_1(t) \exp(-j2\pi f(t - \tau_1'))
\end{aligned} \tag{23}$$

and

$$\begin{aligned}
\eta_2^*(t - \tau_2') &= a_2(t) \exp(j2\pi ft) \exp(-j2\pi f \frac{R_{2,0}}{c}) \exp(j2\pi f_{D,2} t) \\
&= a_2(t) \exp(j2\pi ft) \exp(-j2\pi f \frac{1}{c} (R_{2,0} - |(\mathbf{v}_2 - \mathbf{v}_T)|_{LOS} t)) \\
&= a_2(t) \exp(j2\pi f(t - \frac{R_{2,0}}{c} + \frac{1}{c} |(\mathbf{v}_2 - \mathbf{v}_T)|_{LOS} t)) \\
&= a_2(t) \exp(j2\pi f(t - (\frac{R_{2,0}}{c} - \frac{1}{c} |(\mathbf{v}_2 - \mathbf{v}_T)|_{LOS} t))) \\
&= a_2(t) \exp(j2\pi f(t - (\tau_2 - \frac{f_{D,2}}{f} t))) \\
&= a_2(t) \exp(j2\pi f(t - \tau_2'))
\end{aligned} \tag{24}$$

The forms of τ_1' and τ_2' are given by Equation (14) in which the target-to-receiver distance and the relative Doppler are coalesced together, signifying that both the TDOA and FDOA information are embedded in the measured signals.

The generalized cross-ambiguity function in Equation (19) can then be expressed as [28],

$$\chi(\tau_1', \tau_2') = \int \eta_1(t - \tau_1') \eta_2^*(t - \tau_2') dt \tag{25}$$

Both receivers are detecting the same signal from a moving emitting target at a distance $R_{r,0}$ and seeing a Doppler $f_{D,r}$; the subscripts $r = 1,2$ refer to the two receivers. Introducing a change of variable $t_0 = t - \tau_1$, and re-defining the variable t_0 as t , Equation (25) hence can be rewritten as,

$$\chi(\tau, f_D) = \chi(\tau_1', \tau_2') = \int \eta_1(t) \eta_2^*(t - (\tau_2' - \tau_1')) dt \quad (26)$$

where

$$(\tau_2' - \tau_1') = \frac{(R_{2,0} - R_{1,0})}{c} - \frac{1}{c} [|(\mathbf{v}_2 - \mathbf{v}_T)|_{LOS} - |(\mathbf{v}_1 - \mathbf{v}_T)|_{LOS}] t = \tau - \frac{f_D}{f} t \quad (27)$$

with τ and f_D given by Equation (20). Equation (26) is in the conventional form of the matched filter response function for signal processing. The terms matched filter and ambiguity function are sometimes used interchangeably [29]. Mathematically, Equation (26) is a cross-correlation process.

It is well recognized that the matched filter process can be performed more efficiently in the frequency domain by making use of the power theorem relation [26,29]. Equation (26) can be rewritten as,

$$\chi(\tau, f_D) = \int \eta_1(t) \eta_2^*(t - (\tau_2' - \tau_1')) dt = \int_{\beta} U_1(f) U_2^*(f - f_D) \exp(j2\pi f \tau) df \quad (28)$$

The spectral signal $U(f)$ is the Fourier transform of the temporal signal $\eta(t)$. That is to say, the matched filtering process can be performed simply by a straight-forward multiplication operation of the spectral signal $U(f)$ in the frequency domain over the signal bandwidth β , instead of a correlation in the time domain. It should be noted that in Equation (28), the following approximation is assumed;

$$U_1(f) U_2^*(f - f_D) = U_1(f - f_{D,1}) U_2^*(f - f_{D,2}) \approx U_1(f) U_2^*(f) \quad (29)$$

Equation (29) indicates that both passive receivers see a Doppler shift due to a moving target. However, since the Doppler frequency shift due to relative target-sensor motion is usually very small compare to the radar frequency, i.e., $f \gg f_D$, the multiplication between the two receivers over a given signal spectral bandwidth β is usually a very good approximation since the signal bandwidth is generally much greater than the amount of Doppler shift (i.e., $\beta \gg f_D$). In dealing with measured data, this is equivalent to mixing the in-phase and quadrature (I, Q) signals in the frequency domain from the two receivers [30], i.e.,

$$(I, Q)_n = (I, Q)_{n,1} (I, Q)_{n,2}^* = U_1(f) U_2^*(f) \quad (30)$$

The $(I, Q)_{n,s}$ signals contain the range and Doppler information; they are given by,

$$(I, Q)_{n,s} = A_{n,s} \exp\left(j \frac{2\pi f_n}{c} R_{sT}(t)\right) \quad (31)$$

where $s = 1, 2$ corresponds to receiver S1 and receiver S2 respectively, A is the amplitude of the spectral signal $U(f)$ and subscript n is the frequency index that describes the frequency of the receiver signals spanning over the bandwidth β in the frequency domain such that

$$f_n = f_0 + n\Delta f \quad (32)$$

where f_0 is the initial frequency value and $n = 1, 2, \dots, N-1$, giving an effective bandwidth

$$\beta = (N - 1)\Delta f \quad (33)$$

where Δf is the frequency step size, and N is the number of frequency samples used; i.e., f_0, f_1, \dots, f_{N-1} . Note that although Equation (33) uses the stepped frequency waveform notation, it is also applicable to the spectral content of a temporal mono-pulse signal [24, p. 416], frequency-chirped waveform and continuous-wave frequency-modulated waveform. Annex A gives an illustration of equivalence between stepped-frequency waveform and frequency-chirped waveform to illustrate the general applicability of Equation (33) in modelling signal bandwidth in the frequency domain. Assuming the spectral amplitude A is a constant, a rectangular-shaped spectrum spanning over the signal bandwidth is commonly used in signal and radar analyses. The variable $R_{sT}(t)$ in Equation (31) contains the time-delay and relative target-receiver motion is given in Equation (14).

The TDOA and FDOA information can be processed from the measured (I,Q) data. To process the measured data from a target, the received temporal signals are divided into finite durations commonly known as “slow-time” intervals using Synthetic Aperture Radar (SAR) terminology [29]. A slow-time interval covers at least one signal waveform cycle that contains the signal bandwidth. For example, a signal pulse typically represents one waveform cycle with a given bandwidth. Using the relation given by Equation (28), the matched filter over one slow-time interval can be expressed as,

$$\begin{aligned} \chi(\tau, f_D) &= \int_{\Delta t_s} \eta_1(t) \eta_2^*(t - (\tau_2' - \tau_1')) dt \\ &= \int_{\beta} U_1(f) U_2^*(f) \exp(j2\pi f \tau) df \end{aligned} \quad (34)$$

In other words, the spectral signals clipped from a temporal segment, containing one slow-time interval Δt_s , are analyzed. The digital form of the matched filter output of Equation (34) can be expressed as,

$$H_{m,k} = \sum_{n=0}^{N-1} \left[(I, Q)_n \right]_{\Delta t_S(m)} \exp \left(j \frac{2\pi}{N} nk \right) \quad (35)$$

where the index $m = 1, 2, \dots, M$; the index m indicates the m -th signal sample segment taken from a leg of temporal data. There can be a number of matched filter outputs processed in a temporal sequence for use in FDOA processing. FDOA information can be obtained over a series of H outputs over slow time; $\Delta t(m)$ indicates the m -th slow time of the H output. FDOA will not be discussed in this report; the possibility of processing multiple H outputs is indicated in Equation (35) for completeness. Note that Equations (34) and (35) imply that the time-domain matched filter process is a Fourier transform of the receiver signals in the frequency domain. Matched filter output H contains τ (TDOA) and f_D (FDOA) information as defined in Equation (28). Physically, H can be interpreted as a 1-dimensional target range profile (in SAR terminology) located along the range-difference ($c\tau$) axis somewhere between the two receivers that are deployed to produce the cross-correlation signal. The index k is the range-difference bin number of the target signal profile H ; i.e., $k = 1, 2, \dots, N$. An illustration of H is shown in Figure 6a. Substituting Equation (31) into Equation (35), the range-difference profile of a given signal sample segment can be expressed as [31],

$$H_{m,k}(\tau, f_D) = h_{m,k} \exp \left(j \frac{2\pi f_c}{c} [R_{2T}(t) - R_{1T}(t)]_k \right)_m \quad (36)$$

where $R_{1T}(t)$ and $R_{2T}(t)$ are given by Equation (14) which contain both TDOA (τ) and FDOA (f_D) information via Equation (20). For TDOA application, only the envelop of the range-difference profile $h_{m,k}$ is of interest, and is given by,

$$h_{m,k} = \left| \frac{A}{N} \frac{\sin(N\alpha/2)}{\sin(\alpha/2)} \exp(j \frac{N-1}{N} \pi k) \right| \quad (37)$$

where

$$\alpha = \frac{2\pi(R_{2T}(t) - R_{1T}(t))}{(c/\beta)N} + \frac{2\pi k}{N} \quad (38)$$

and A is the spectral amplitude of the mixed (I, Q) signals; f_c is the band centre frequency. The envelop of the profile is given by $\sin(N\alpha/2)/\sin(\alpha/2)$. The width of the profile envelop is determined by the bandwidth β of the target signal; a wider bandwidth produces a narrower profile. The spacing between adjacent range-difference bins ($k, k+1$) is given by c/β [33]. The peak value of the profile given in Equation (37) is the TDOA measurement value d_{ij} that is sought, and has units in meters (see Equation (1)).

3.3 TDOA measurement errors

Target location is obtained by solving the set of TDOA equations in Equation (1). TDOA measurements (d_{ij}) are needed as target information input into Equation (1) to solve for x , y , z . However, errors introduced in the TDOA measurements will affect the accuracy of target localization [1,3,8,12]. The errors in the TDOA measurements processed through a cross-correlator can be described statistically by the Cramer-Rao Lower Bound variance [22,24,25],

$$\sigma^2 \geq \left(2 \frac{E}{N_0} B^2 \right)^{-1} \quad (39)$$

where E is the signal energy [J], N_0 is the noise spectral power density [W/Hz], and B [Hz] is a width measure of the signal bandwidth. It can be seen that the errors are dependent on the signal and noise levels and the signal's bandwidth. To analyze the signal and noise effect, zero-mean white Gaussian noise can be added to the signals in Equation (34) [22,23,24]; i.e.,

$$u_s(t) = \eta_s(t) + N_s(t) \quad (40)$$

where $u(t)$ is the signal with added noise, $\eta(t)$ is the signal, and $N(t)$ is the additive white Gaussian noise, subscript s denotes the s -th receiver in the detection system. The width measure of the signal's bandwidth is given by [22],

$$\begin{aligned} B^2 &= \frac{(2\pi)^2 \int_{-\infty}^{\infty} f^2 |U(f)|^2 df}{\int_{-\infty}^{\infty} |U(f)|^2 df} \\ &= \frac{(2\pi)^2 \int_{-\beta/2}^{\beta/2} f^2 |U(f)|^2 df}{\int_{-\beta/2}^{\beta/2} |U(f)|^2 df} = \frac{\pi^2 \beta^2}{3} \end{aligned} \quad (41)$$

assuming the signal energy density spectrum $|U(f)|^2$ is a rectangular-shaped function of unit height with a width β , the signal's bandwidth [Hz].

The expression for the Cramer-Rao Lower Bound for the TDOA measurement error has been given in different forms from various analyses in the literature; it has been shown that all these different expressions can be re-expressed in a common form [25]. This form of the Cramer-Rao Lower Bound error is given as [22],

$$\sigma \geq \frac{1}{\beta \sqrt{(2\pi^2 / 3) \beta_{noise} T(S/N)}} = \frac{1}{\beta \sqrt{6.5 (S/N)_T}} \quad (42)$$

where $T = E/S$ is the signal integration time [s], S is the signal power [W], β_{noise} is the receiver noise bandwidth [Hz], and $N = N_0\beta_{noise}$ is the noise power [W]; note that σ has units in seconds [s]. S/N is the input signal-to-noise ratio (SNR) to the cross-correlator given in Equation (28). The factor $(S/N)_T = \beta_{noise}T(S/N)$ in the denominator in Equation (42) can be thought of as the time-integrated output SNR of the correlated signal processed through the cross-correlator.

An output of a range-difference target profile signal in the absence of noise as given by Equation (36) is shown in Figure 6a. The same signal with a $(S/N)_T = 16$ (12 dB) is shown in Figure 6b; note that the SNR at detection threshold is nominally set at around 12 dB in practice [22,32]. It is obvious from Figure 6a that in the case where noise is absent, the noise-free signal trace is very definitive; therefore, the location of the signal peak representing the TODA measurement value (d_{ij}) can be determined precisely. When noise is present in the signal (Figure 6b), the location of the peak is much less definitive. Figure 7 shows a superposition of twenty samples of noisy target profiles with a detection SNR, $(S/N)_T = 12$ dB. Clearly, each target profile with a random noise structure has a somewhat varying peak location. The variation in the peak's location is confined to within the width of the signal profile H (Equation (36)) as defined by the bandwidth β , and the amount varied from the actual peak is dependent on the detection SNR factor $(S/N)_T$ as given by the Cramer-Rao Lower Bound standard deviation, σ . It can be interpreted as a statistical estimate of an average deviation (i.e., a root mean square error) of a signal peak location of the target along the range-difference axis.

From Equation (42), the standard deviation ε in the measurement from the error-free TDOA value can be rewritten as (in spatial units, meters),

$$\varepsilon = c\sigma \geq \frac{c}{\beta\sqrt{6.5(S/N)_T}} = \frac{\Delta r}{\sqrt{6.5(S/N)_T}} \quad (43)$$

where c is the speed of light, and $\Delta r = c/\beta$ is defined as the resolution cell spacing [33] of the range-difference profile given by Equation (36). A resolution cell in the context here is referring to the separation distance between two adjacent range-difference bins, and not the Rayleigh's criterion conventionally used in defining image resolution.

It is seen from Equation (43) that a variation in the measurement by an amount ε will result in a TDOA measurement with error; ε is a function of both the signal bandwidth β and the cross-correlator output SNR $(S/N)_T$. When the signal bandwidth is wide, the target profile envelope of Equation (37) will be narrow; this pinpoints better the signal peak location. When the output SNR value $(S/N)_T$ is very large, this means the target profile will appear as a very clean trace, approaching the one shown in Figure 6a. Hence a precise peak location can be determined. Both a wide signal bandwidth β , and a large SNR output $(S/N)_T$ will reduce the TDOA measurement error.

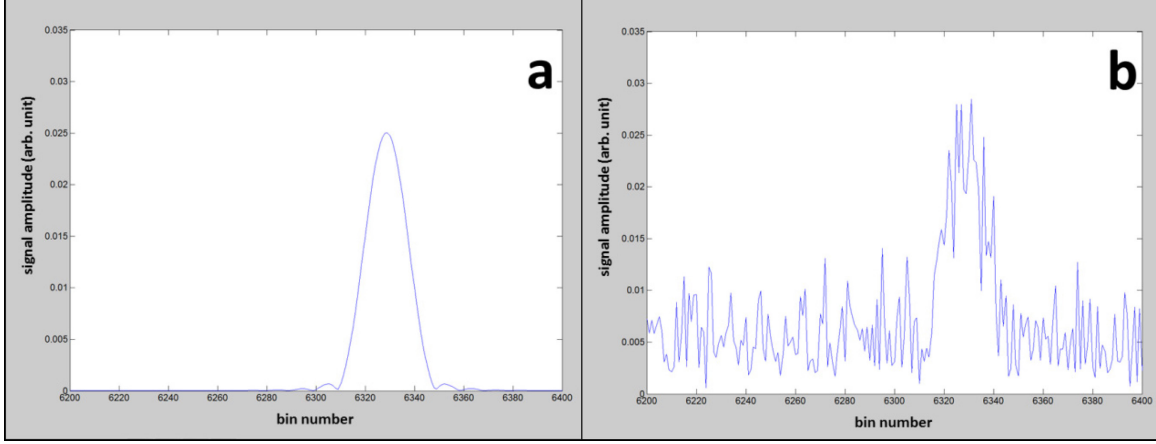


Figure 6: a) a range-difference profile signal without noise; b) with noise SNR = 12 dB.

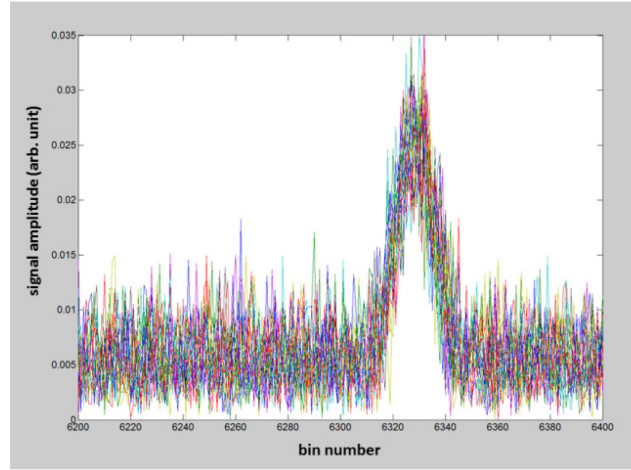


Figure 7: Superposition of twenty range-difference profile signals with noise, SNR = 12 dB.

3.3.1 TDOA measurement error modelling

Using Equation (43), the amount of TDOA measurement with error (d_{ij}) can be modelled by incorporating the bandwidth β and the cross-correlator output SNR $(S/N)_T$ information into the Fourier transform process in Equation (35) that generates the range-difference signal envelope h in Equation (37). The accuracy of the signal profile peak's location (i.e., TDOA measurement) is determined by the ability to measure the resolution cell spacing $\Delta r = c/\beta$ from the sampled signals, and the spacing within a resolution cell can be further sub-divided into smaller graduation (i.e., finer granularity) by inserting extra bins through the zero-padding process in the Fourier transform. Thus the effective spacing between two adjacent bins of the signal envelope h in Equation (37) can be expressed as,

$$\Delta r_z = \frac{\Delta r}{N_z} = \frac{c}{\beta N_z} \quad (44)$$

where N_z is the zero-padding multiplier to increase the number of bins in the Fourier transform operation in Equation (35). A smaller Δr_z provides finer sampling of h , hence a more accurate the peak location of h can be obtained. It should be emphasized that the intrinsic resolution Δr of the envelope h as defined by the Rayleigh's criterion is not altered.

Comparing the forms of Equation (44) and Equation (43), it can be seen that the part of the Cramer-Rao Lower Bound that is given by $(S/N)_T$ can be modelled by putting the appropriate amount of zero-padding in the Fourier transform of Equation (35); i.e., the zero-padding multiplier is expressed as,

$$N_z = \sqrt{6.5(S/N)_T} \quad (45)$$

That is to say, zero-padding provides a finer granularity in measuring h , hence better TDOA measurement accuracy. Since noise present in the signal is assumed to be zero-mean white Gaussian [24], the average of a large collection of noisy profiles will statistically average out to the original noiseless profile. Hence, this is consistent with the model described here in which the average of a large number of noisy h profiles can be represented by a clean (noiseless) target profile.

The statistical TDOA measurement error is then modelled as a function of the bandwidth parameter β , and the SNR parameter $(S/N)_T$ in the cross-correlation process. This translates to location error of the signal profile peak based on how fine the peak of h can be measured along the range-difference axis. The TDOA measurement value d_{ij} with error included can be determined from the signal profile peak's location as,

$$d_{ij} = c\tau = 2x = (bin\#_{peak} - bin\#_{mid-pt}) \Delta r_z \quad (46)$$

where x is the x-coordinate along the range-difference profile; $bin\#_{peak}$ is peak of the h envelope given by Equation (37) (see also Figure 6), and $bin\#_{mid-pt}$ is the zero point ($x = 0$) of the range-difference axis. Thus, the TDOA measurement d_{ij} with an error of about ε (Equation (43), i.e., "one sigma") is modelled by β and $(S/N)_T$ as given in the Cramer-Rao Lower Bound in the cross-correlation outputs.

3.3.2 Computing TDOA measurements with errors

An assessment of the estimated TDOA measurements with their associated errors from the signal profile peak's location method as discussed in Section 3.3.1 is conducted. Different values of β , and $(S/N)_T$ are used to evaluate the validity of the TDOA measurement error obtained by the above modelling method.

For comparison purposes, a set of three error-free TDOA measurement values (d_{ij}) are extracted from the scenario in Figure 1 as reference sets. Since the target's flight path (ground truth) and the receiver locations are known a-priori, error-free d_{ij} values can be calculated from Equation (1). The receivers are set up in a coplanar system configuration where they all lie on a flat plane at $z=0$. Signals from the target are taken at regular time intervals. The d_{ij} values are

calculated at ten different time instants from the three pairs of receivers, S1-S2, S3-S4 and S1-S4 that form the passive receiver system. These error-free TDOA measurement values are tabulated in Table 1. They will be used in Section 4 to analyze the performance of target localization accuracy.

Table 1: TDOA measurement values with no errors.

Time (time index)	TDOA1 (d_{12}) [m]	TDOA2 (d_{34}) [m]	TDOA3 (d_{14}) [m]
1	-2131.36	1548.64	-789.87
2	-1988.87	1416.33	-776.71
3	-1821.73	1263.33	-759.11
4	-1624.42	1085.32	-735.75
5	-1390.25	877.10	-704.95
6	-1111.39	632.51	-664.82
7	-779.20	344.49	-613.45
8	-385.08	5.50	-549.26
9	78.01	-391.72	-471.74
10	613.25	-852.65	-382.01

Since the modelling error is inversely proportional to the product βN_z in the Cramer-Rao Lower Bound as according to Equation (44), both the bandwidth parameter β and the SNR parameter $(S/N)_T$ can be varied to provide an assessment of their effect on the TDOA measurement error. To avoid being overly cumbersome, and without any loss of generality in the analysis, $(S/N)_T$ is set as a constant value, and only the bandwidth parameter β is varied in the assessment; for example, $\beta = 1, 20$ and 300 MHz respectively are investigated. A value of $(S/N)_T = 16$ (12 dB) is used; this corresponds to the nominal detection threshold value of 12 dB as discussed in Section 3.3.

Using these values, the TDOA measurement error ε based on the Cramer-Rao Lower Bound in Equation (43) is tabulated in Table 2. The bandwidth range covering 1 to 20 MHz gives a reasonable coverage of many real-world signals encountered. For example, UAV control-link and communication signals require a bandwidth of about 2 MHz [32]; high-definition TV transmission signals are carried either by a bandwidth $\beta = 6$ MHz (North America) or a bandwidth $\beta = 20$ MHz (Asia) [34]. First-person-view piloting signal for drones transmits a bandwidth of 15 MHz [35]. The case of $\beta = 300$ MHz corresponds to an air platform carrying an imaging radar for Synthetic Aperture Radar (SAR) applications; SAR radars have very wide bandwidths, generally up to 1 GHz [36].

Table 2: Cramer-Rao Lower Bound rms error ε for different signal bandwidth values.

β	$(S/N)_T$	ε
1 MHz	12 dB	30 m
20 MHz	12 dB	1.5 m
300 MHz	12 dB	0.1 m

The TDOA measurements for signal bandwidth $\beta = 1$ and 20 MHz are shown in Table 3 and Table 4 respectively. The bracketed values are the errors in the TDOA measurements (d_{ij}) in comparison with the reference error-free d_{ij} values in Table 1. It can be seen from Tables 3 and 4 that the TDOA measurement errors (bracketed values) are spreading roughly to the “one-sigma”

point ε as a bound (see Table 2 for values of ε). There are some instances when the error is larger than “one sigma”. This is a consequence of a moving target with changing temporal phase through the Fourier transform operation; as a result, the profile peak could be shifted by one range-difference bin in the cross-correlation process, resulting in a bigger error. As the bandwidth β increases from 1 to 20 MHz, the TDOA measurement errors decrease in accordance to the reduction in ε .

Note that the errors (bracketed values) in the TDOA measurements (d_{12} , d_{34} , d_{14}) in Tables 3 and 4 vary randomly among the three TDOA sets and among different target positions. The cross-correlator that generates the TDOA measurements as outputs is seen to be sensitive to the orientation between the receiver-pairs and the target positions. The variations of errors are determined by the Cramer-Rao Lower Bound ε value.

Table 3: TDOA measurements for signal with $\beta = 1$ MHz and $(S/N)_T = 12$ dB.

Time (time index)	TDOA1 (d_{12}) [m]	TDOA2 (d_{34}) [m]	TDOA3 (d_{14}) [m]
1	-2130 (+1.36)	1530 (-18.64)	-780 (+9.87)
2	-1980 (+8.87)	1410 (-6.33)	-780 (-3.29)
3	-1800 (+21.73)	1260 (-3.33)	-750 (+9.11)
4	-1620 (+4.42)	1080 (-5.32)	-720 (+15.75)
5	-1380 (+10.25)	870 (-7.10)	-690 (+14.95)
6	-1080 (+31.39)	600 (-32.5)	-660 (+4.82)
7	-750 (+29.20)	330 (-14.49)	-600 (+13.45)
8	-360 (+25.08)	-30 (-35.5)	-540 (+9.26)
9	120 (+41.99)	-420 (-28.28)	-480 (-8.26)
10	660 (+46.75)	-870 (-17.35)	-390 (-7.99)

Table 4: TDOA measurements for signal with $\beta = 20$ MHz and $(S/N)_T = 12$ dB.

Time (time index)	TDOA1 (d_{12}) [m]	TDOA2 (d_{34}) [m]	TDOA3 (d_{14}) [m]
1	-2128.50 (+2.86)	1546.50 (-2.14)	-789.00 (+0.87)
2	-1986.00 (+2.87)	1414.50 (-1.83)	-775.50 (+1.21)
3	-1819.50 (+2.23)	1261.50 (-1.83)	-759.00 (+0.11)
4	-1621.50 (+2.92)	1083.00 (-2.32)	-735.00 (+0.75)
5	-1387.50 (+2.75)	876.00 (-1.1)	-703.50 (+1.45)
6	-1110.00 (+1.39)	631.50 (-1.01)	-664.50 (+0.32)
7	-777.00 (+2.20)	343.50 (-0.99)	-612.00 (+1.45)
8	-384.00 (+1.08)	4.50 (-1.0)	-549.00 (+0.26)
9	79.50 (+1.49)	-393.00 (-1.28)	-471.00 (+0.74)
10	615.00 (+1.75)	-853.50 (-0.85)	-381.00 (+1.01)

To further verify that the modelling of the error ε in the Fourier transform of the cross-correlation process is reasonable and valid, the bandwidth β is increased to 300 MHz; that would decrease the Cramer-Rao Lower Bound error ε to 0.1 m (see Table 2). The TDOA measurements obtained for a signal bandwidth $\beta = 300$ MHz confirms that the measurement errors (bracketed values) are indeed very small, bounded approximately by the “one-sigma” point. This is shown in Table 5.

Table 5: TDOA measurements for signal with $\beta = 300$ MHz and $(S/N)_T = 12$ dB.

Time (time index)	TDOA1 (d_{12}) [m]	TDOA2 (d_{34}) [m]	TDOA3 (d_{14}) [m]
1	-2131.10 (+0.26)	1548.50 (-0.14)	-789.80 (+0.07)
2	-1988.60 (+0.27)	1416.20 (-0.13)	-776.60 (+0.11)
3	-1821.50 (+0.23)	1263.20 (-0.13)	-759.00 (+0.11)
4	-1624.20 (+0.22)	1085.20 (-0.12)	-735.70 (+0.05)
5	-1390.10 (+0.15)	877.00 (-0.10)	-704.90 (+0.05)
6	-1111.20 (+0.19)	632.40 (-0.11)	-664.80 (+0.02)
7	-779.00 (+0.20)	344.40 (-0.09)	-613.40 (+0.05)
8	-384.90 (+0.18)	5.40 (-0.1)	-549.20 (+0.06)
9	78.10 (+0.09)	-391.80 (-0.08)	-471.70 (+0.04)
10	613.30 (+0.05)	-852.70 (-0.05)	-382.00 (+0.01)

4 Target location by intersection of hyperboloids

In this section, a discussion is given on solving the TDOA equations shown in Equation (1) using the geometric approach described in Section 2. Hyperboloids are generated based on TDOA measurement values d_{ij} processed from the signals collected by the receivers as discussed in Section 3.3.2. Target localization is then obtained by finding where the hyperboloids intersect as a solution to Equation (1).

The target localization accuracy problem due to TDOA measurement errors will be investigated using two different receiver configurations. A coplanar set-up in which all four receivers in the detection system are placed on the same geometric plane (e.g., the height coordinate z is the same for all the receivers), and a non-coplanar set-up in which one of the receivers is out of the common plane of the other receivers (e.g., the z coordinate of one receiver is different from that of the other receivers) will be examined. Numerical results from both coplanar and non-coplanar systems will offer a better picture on how system geometry can be utilized to obtain more accurate target localization.

4.1 Locating target with coplanar receivers

A coplanar receiver configuration is one in which all four receivers are lying on a common receiver plane (e.g., at $Z_i = 0$; $i = 1,2,3,4$). The geometric layout of the coplanar configuration is given in Table 6. X_i, Y_i, Z_i denote the known receivers coordinates. It corresponds to the set-up illustrated in Figure 1. TDOA measurements from the three receiver-pairs are converted to three hyperboloids with respect to the local coordinate frame of each receiver-pair as described in Section 2.3. In order to find the target location, the three hyperboloids have to be put into a common global coordinate frame and re-oriented accordingly to the system geometry so that the intersection of the three hyperboloids can be determined.

Table 6: Ground-truth locations of receivers in global coordinates.

Configuration:	Coplanar			Non-coplanar		
Receivers	X [m]	Y [m]	Z [m]	X [m]	Y [m]	Z [m]
S1	-5000	3400	0	-5000	3400	0
S2	-1600	0	0	-1600	0	200
S3	1600	0	0	1600	0	0
S4	5000	3400	0	5000	3400	0

4.1.1 Putting the hyperboloids in global coordinate frame

Using receiver-pair S1-S2 as an illustrative example, the procedure for transforming a hyperboloid from its local frame (x',y',z') to the global frame (x,y,z) is performed as follows. First, the $x'-z'$ axes at $y'=0$ of the local frame is overlaid parallel to the $x-z$ axes at $y=0$ of the global frame. This effectively re-labels the coordinates of sensors S1, S2 and the associated hyperboloid from (x',y',z') to (x,y,z) ; i.e., $x' \rightarrow x, y' \rightarrow y, z' \rightarrow z$. With the re-labelling of the axes, receivers S1 and S2 are now situated on the x -axis in the global frame. In other words, (X'_1, Y'_1, Z'_1) becomes

(X_l, Y_l, Z_l) for receiver S1, (X_2', Y_2', Z_2') becomes (X_2, Y_2, Z_2) for receiver S2, and (x', y', z') becomes (x, y, z) for the hyperboloid associated with receiver-pair S1-S2. The task is then to re-locate the two receivers and the associated hyperboloid from the local coordinate position (Figure 4) to its proper location in the global coordinate frame (Figure 1b), conforming to the receiver system configuration in Table 6. That is to say, since the hyperboloid is fixed in position relative to the positions of receivers S1 and S2, the hyperboloid will move in the exact same manner as moving the two receivers from the locations in local coordinate frame to locations in the common global coordinate frame as given in Table 6 (coplanar case) through a series of translations and rotations. By overlaying the local frame onto the global frame, receivers S1 and S2 have initial position coordinates as given in Table 7 but with coordinates $(X_l, Y_l, Z_l) = (-2404.15, 0, 0)$ and $(X_2, Y_2, Z_2) = (2404.15, 0, 0)$ respectively. Note that the separation distance d (4804.3.m) between S1 and S2 is the same between Table 6 (coplanar case) and Table 7.

Table 7: Receivers S1 and S2 locations in local coordinate frame.

Receivers	X' [m]	Y' [m]	Z' [m]
S1	-2404.15	0	0
S2	2404.15	0	0

To begin the transforming process, the receiver-pair (S1-S2) and its associated hyperboloid (collectively referred to as the “ensemble” hereafter) is first translated such that S2 at $(d/2, 0, 0)$ is moved to $(x, y, z) = (0, 0, 0)$; i.e.,

$$\begin{aligned} x_{new1} &= x - \frac{d}{2} \\ y_{new1} &= y \\ z_{new1} &= z \end{aligned} \tag{47}$$

Receiver S2 is then acted as the pivot to rotate the whole ensemble about the z-axis. A rotation in the clockwise direction by an angle,

$$\phi = \arctan\left(\frac{Y_1 - Y_2}{X_1 - X_2}\right) \tag{48}$$

is performed, where (X_l, Y_l, Z_l) and (X_2, Y_2, Z_2) are the ground truth locations of receivers S1 and S2 in the global frame as given in Table 6. The clockwise-rotated coordinates of the ensemble are given by,

$$\begin{aligned} x_{new2} &= x_{new1} \cos(-\phi) - y_{new1} \sin(-\phi) \\ y_{new2} &= x_{new1} \sin(-\phi) + y_{new1} \cos(-\phi) \end{aligned} \tag{49}$$

This provides the proper orientation of the receiver-pair S1-S2 with respect to the x-axis in the x-y plane. The final position of the ensemble is arrived at through a translation,

$$\begin{aligned}
x_{final} &= x_{new2} + X_2 \\
y_{final} &= y_{new2} + Y_2 \\
z_{final} &= z_{new2} + Z_2
\end{aligned} \tag{50}$$

The same procedure above is applied to receiver-pair S3-S4 to put its associated hyperboloid in the global coordinate frame. S3 is first translated to $(x,y,z) = (0,0,0)$ to serve as a rotating pivot. The receivers-hyperboloid ensemble is rotated counter-clockwise by an amount ϕ , and then translated to the final position relative to the ground truth location of S3, (X_3, Y_3, Z_3) . For the third receiver-pair (S1-S4) and its corresponding hyperboloid, the final positions are obtained simply by a translation in the positive y-axis direction by an amount Y_l .

4.1.2 Error-free TDOA measurements as reference

To see how TDOA measurement error affects target localization accuracy, it is helpful to first establish a case study in which the measurements contain no error as reference so that comparison can be made with cases where errors are present. Using the error-free TDOA measurement values (d_{ij}) from Table 1 for the coplanar receiver set-up, a set of three hyperboloids is computed using Equation (5) at each of the ten time instants along the target's flight path; target localizations are then extracted from the intersection of the three hyperboloid surfaces at all ten time instants to generate a target track. The intersection point is determined by scanning the target altitude z with an increment of 1 m for a range of altitude from $z = 0$ to 2000 m. At each altitude z , Equation (1) in the form of a residual quantity given by,

$$S = \sum_q |d_{ij} - (r_i - r_j)|_{q(i,j)} \tag{51}$$

is computed. The altitude z where S is closest to zero is the point of intersection of the three hyperboloids, pinpointing the target location in x, y, z [16]. That is, a minimum S is sought along the z -direction to pinpoint the intersection of the three hyperboloids. The subscript q is an index indicating the three receiver-pairs (i,j) used in the TDOA measurements, e.g., $q(1,2) = 1$, $q(3,4) = 2$, $q(1,4) = 3$.

Table 8 shows the computed target localization results (x,y,z) and the target ground truths (X_{Tg}, Y_{Tg}, Z_{Tg}) for comparison. The results indicate that the computed target locations are accurate to within 1 m in altitude z , the increment size of the altitude scan; the computed (x,y) coordinates are identical to the ground truth values. Thus, for all practical intents and purposes, the computed results show that the three hyperboloids do intersection at a point when there is no error in the TDOA measurements d_{ij} , hence providing very accurate target localization in x, y, z . A graphical illustration of three intersecting hyperboloids is shown in Figure 8. A z -slice of the intersecting hyperboloids at the actual target altitude $z = 1000$ m is shown in Figure 9; it shows that the three hyperbolic curves are intersecting at a point.

Table 8: Comparisons of target localization from error-free TDOA measurements and target ground-truth positions for coplanar receiver system.

Time (time index)	Target ground truths [m]			Computed target locations [m]		
	X_{Tg}	Y_{Tg}	Z_{Tg}	x	y	z
1	-660.00	9998.50	1000.00	-660.00	9998.50	1000.00
2	-608.44	9328.48	1000.00	-608.44	9328.48	1000.00
3	-556.89	8658.46	1000.00	-556.89	8658.46	1000.00
4	-505.33	7988.44	1000.00	-505.33	7988.44	1000.00
5	-453.78	7318.42	1000.00	-453.78	7318.42	1000.00
6	-402.22	6648.40	1000.00	-402.22	6648.40	1000.00
7	-350.67	5978.38	1000.00	-350.67	5978.38	1000.00
8	-299.11	5308.36	1000.00	-299.11	5308.36	1000.00
9	-247.56	4638.34	1000.00	-247.56	4638.34	1000.00
10	-196.00	3968.32	1000.00	-196.00	3968.32	1000.00

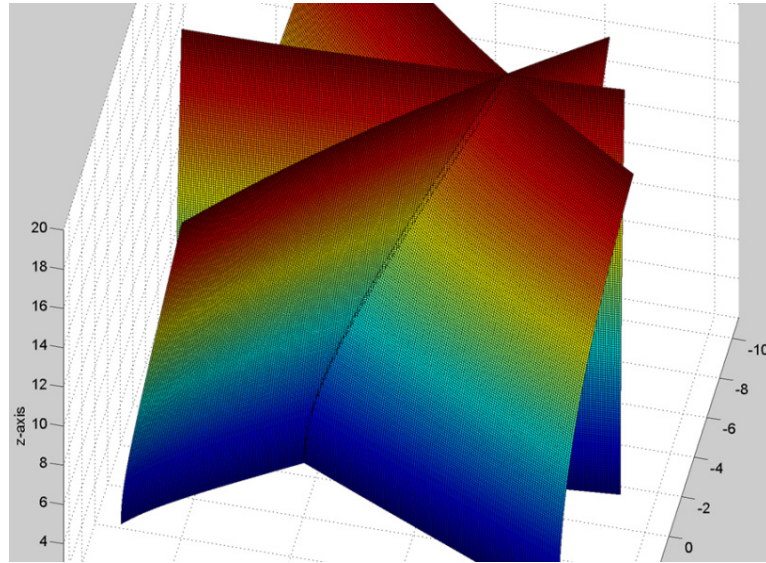


Figure 8: Three intersecting hyperboloids from three TDOA measurements.

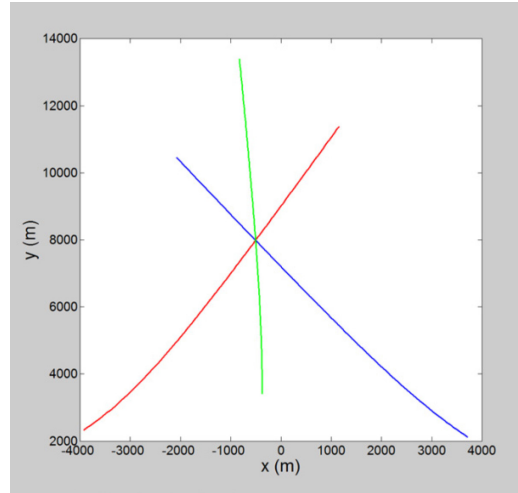


Figure 9: Intersection of three hyperbolic curves at a slice of target altitude, $z = 1000$ m.

4.1.3 Target localization from TDOA measurements with errors

For signals with finite bandwidths and moderate SNR, the TDOA measurements d_{ij} will contain errors from the variance given by the CRLB as discussed in Section 3.3. For signals with a bandwidth, $\beta = 1$ MHz and $(S/N)_T = 12$ dB (or 16), the TDOA measurement with error values d_{ij} and the amounts deviated from the error-free values (bracketed) are shown in Table 3 of Section 3.3.2. Using the d_{ij} values in Table 3, the computed target localization results are shown in Table 9 below. It can be seen that the computed target's track positions (x,y) are offset considerably compared to the ground truth (X_{Tg}, Y_{Tg}) . In particular, the computed target altitude z has very large errors comparing to the ground truth Z_{Tg} . The source of this large altitude error is found to be a consequence of the receiver system's coplanar configuration; a remedy to this problem will be discussed later in Section 4.2.

Table 9: Comparisons of target localization from TDOA measurements with errors and actual target positions for coplanar receiver system. CRLB parametric values used: $\beta = 1$ MHz and $(S/N)_T = 12$ dB.

Time (time index)	Target ground truths [m]			Computed target locations [m]		
	X_{Tg}	Y_{Tg}	Z_{Tg}	x	y	z
1	-660.00	9998.50	1000.00	-649.17	9889.12	0
2	-608.44	9328.48	1000.00	-700.88	9881.41	3660.00
3	-556.89	8658.46	1000.00	-803.17	10144.20	6610.00
4	-505.33	7988.44	1000.00	-490.19	7932.89	0
5	-453.78	7318.42	1000.00	-438.48	7262.07	0
6	-402.22	6648.40	1000.00	-391.61	6549.75	0
7	-350.67	5978.38	1000.00	-485.88	6316.99	5650.00
8	-299.11	5308.36	1000.00	-292.53	5252.69	0
9	-247.56	4638.34	1000.00	-242.15	4595.37	0
10	-196.00	3968.32	1000.00	-187.34	3950.14	0

Reducing the TDOA errors by increasing the signal bandwidth $\beta = 20$ MHz, and with a $(S/N)_T = 16$, the d_{ij} values are shown in Table 4 of Section 3.3.2. Using these d_{ij} values, Table 10 shows the computed target localization results. The computed target track positions (x,y) are much closer to the ground truth (X_{Tg}, Y_{Tg}) by reducing the TDOA errors. But the target's estimated altitude z is still suffering considerable error; especially at time instants $t = 8$ and 9, the computed altitude z values are off by nearly 100% from the ground truth Z_{Tg} values as seen in Table 10.

Table 10: Comparisons of target localization from TDOA measurements with errors and actual target positions for coplanar receiver system. CRLB parametric values used: $\beta = 20$ MHz and $(S/N)_T = 12$ dB.

Time (time index)	Target ground truths [m]			Computed target locations [m]		
	X_{Tg}	Y_{Tg}	Z_{Tg}	x	y	z
1	-660.00	9998.50	1000.00	-659.84	9994.90	1080.00
2	-608.44	9328.48	1000.00	-609.10	9332.24	1130.00
3	-556.89	8658.46	1000.00	-561.09	8678.75	1270.00
4	-505.33	7988.44	1000.00	-504.69	7981.44	1020.00
5	-453.78	7318.42	1000.00	-461.56	7355.42	1520.00
6	-402.22	6648.40	1000.00	-403.99	6653.53	1150.00
7	-350.67	5978.38	1000.00	-353.01	5984.02	1250.00
8	-299.11	5308.36	1000.00	-293.74	5301.20	0
9	-247.56	4638.34	1000.00	-258.45	4619.69	1900.00
10	-196.00	3968.32	1000.00	-193.72	3976.66	720.00

Increasing the signal bandwidth to $\beta = 300$ MHz, and with a $(S/N)_T = 16$, the TDOA errors are further reduced. The corresponding d_{ij} values are shown in Table 5. Using these TDOA values, Table 11 shows that the computed target positions (x,y) are very close to the ground truth (X_{Tg}, Y_{Tg}) values. The computed target altitude z has also improved in accuracy and is closer to the ground truth Z_{Tg} values. But the error is still sizeable, in tens of meters in the z direction compare to just a few meters in the x and y directions as seen in Table 11. From these three cases, it can be clearly seen that the accuracy in target localization is improving with a reduction in the TDOA measurement errors.

Table 11: Comparisons of target localization from TDOA measurements with errors and actual target positions for coplanar receiver system. CRLB parametric values used: $\beta = 300$ MHz and $(S/N)_T = 12$ dB.

Time (time index)	Target ground truths [m]			Computed target locations [m]		
	X_{Tg}	Y_{Tg}	Z_{Tg}	x	y	z
1	-660.00	9998.50	1000.00	-661.27	10006.95	1080.00
2	-608.44	9328.48	1000.00	-609.30	9333.99	1060.00
3	-556.89	8658.46	1000.00	-557.08	8659.63	1020.00
4	-505.33	7988.44	1000.00	-506.18	7992.80	1060.00
5	-453.78	7318.42	1000.00	-453.87	7318.73	1010.00
6	-402.22	6648.40	1000.00	-403.26	6652.16	1080.00
7	-350.67	5978.38	1000.00	-352.24	5982.43	1130.00
8	-299.11	5308.36	1000.00	-300.97	5310.12	1170.00
9	-247.56	4638.34	1000.00	-248.18	4637.28	1070.00
10	-196.00	3968.32	1000.00	-196.14	3967.43	1020.00

It is interesting to note that even though the computed target altitude has a sizable error, the computed target position (x, y) are rather accurate. Using the case where the signal bandwidth $\beta = 20$ MHz as an example, Figure 10 shows graphically the computed target positions (red diamonds) and the target's ground truth (black circles) that are tabulated in Table 10. The good agreements in target track positions (x, y) can be explained by the fact that the hyperboloid surfaces have relatively flat curvatures along the vertical near the bottom of the intersecting hyperboloids in Figure 8. A target at a low altitude is located near the bottom part of these hyperboloids. The flat curvatures of the hyperboloids in this region mean that even a sizeable change in z does not produce a significant deviation in x or y .

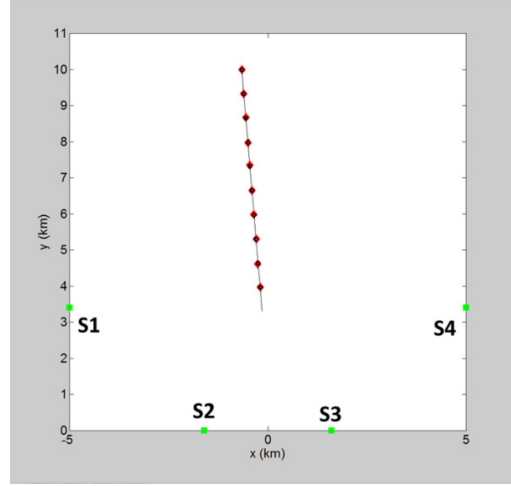


Figure 10: Comparison between computed target track (red diamonds) and ground truth (black circles). CRLB parametric values used: $\beta = 20$ MHz, $(S/N)_T = 12$ dB.

The notable error in the computed target altitude z can be explained as a consequence of the coplanar receiver system configuration. It has been pointed out that coplanar system may not be a desirable configuration to provide accurate three-dimensional target localization [10,14,20]. Reference [20] probably offers the best quantitative explanation using analysis of the algebraic approach to the TDOA solution. Referring to Equation (9) in Section 2.4, the unknown target location (x,y,z) can be solved unambiguously only if the 4×4 matrix has a full rank of 4. That is, at least one of the $(Z_i - Z_l)$ variables in the fourth column in Equation (9) is non-zero. Thus when all the receivers are placed on the same plane at $Z_i = 0$ ($i = 2,3,4,5$), all the $(Z_i - Z_l)$ variables on the fourth column of Equation (9) become zeros. Effectively, Equation (9) is reduced to Equation (10). Moreover, if the TDOA measurements d_{2l} , d_{3l} , d_{4l} contain errors, then Equation (10) becomes ill-conditioned and the solution for $(\|\mathbf{R}_l - \mathbf{R}\|, x, y)$ would become less accurate [16]. This tends to amplify the inaccuracy of the solution for z since it is determined in terms of the solved variables $\|\mathbf{R}_l - \mathbf{R}\|$, x , and y ; i.e.,

$$z = Z_1 - \left(\|\mathbf{R}_1 - \mathbf{R}\|^2 - (X_1 - x)^2 + (Y_1 - y)^2 \right)^{1/2} \quad (52)$$

4.2 Locating target with non-coplanar receivers

It is seen from the results above that the coplanar receiver configuration does not provide very accurate target localization outputs, especially the target altitude z , when the TDOA measurements contain errors. It has been recognized that four receivers in a non-coplanar configuration [9,14,20] is needed for a good target location fix. An investigation of target localization using four receivers in a non-coplanar configuration is thus conducted to assess its performance. A non-coplanar system with four receivers is obtained when receiver S2 is raised to a height $Z_2 = 200$ m; this is shown in Table 6. TDOA measurements with errors are generated for the non-coplanar system case using the same bandwidth and SNR values for the Cramer-Rao Lower Bound as in the coplanar cases (Tables 9, 10, 11). Computations are run and the differences in the target localization results between the coplanar and non-coplanar receiver configurations are compared.

4.2.1 Non-coplanar receivers in the global coordinate frame

As in the coplanar case, the receiver(S1-S2)-hyperboloid ensemble will be used as an example to illustrate the procedure for transforming the hyperboloid from the local coordinate frame to the global coordinate frame. To account for the tilt of the hyperboloid as a result of receiver S2 being raised above the ground (i.e., non-coplanar), an additional rotation for the hyperboloid associated with the S1-S2 receiver-pair has to be performed in the x - z plane. Going through the same procedure as previously described for the coplanar case in Section 4.1.1, the receivers-hyperboloid ensemble is first translated such that receiver S1 is moved to $(x,y,z) = (0,0,0)$; i.e.,

$$\begin{aligned} x_{new} &= x_{old} + \frac{d}{2} \\ y_{new} &= y_{old} \\ z_{new} &= z_{old} \end{aligned} \tag{53}$$

where d is the separation distance between receivers S1 and S2. In the non-coplanar configuration, this separation distance is given by $d = ((X_1 - X_2)^2 + (Y_1 - Y_2)^2 + (Z_1 - Z_2)^2)^{1/2}$. (X_1, Y_1, Z_1) and (X_2, Y_2, Z_2) are the ground truth locations of receivers S1 and S2 respectively in the global frame as given in Table 6 (non-coplanar case). Receiver S1 at the new location serves as the pivot to rotate the hyperboloid in the x - z plane. Recall that this translation operation provides the same movement on the receivers and on the hyperboloid simultaneously. The hyperboloid is then rotated in the x - z plane in the counter-clockwise direction by an angle,

$$\theta = \arctan \left(\frac{Z_2 - Z_1}{((X_2 - X_1)^2 + (Y_2 - Y_1)^2)^{1/2}} \right) \tag{54}$$

A rotation of the ensemble pivoting about S1 is given by,

$$x_{new2} = x_{new} \cos \theta - z_{new} \sin \theta \quad (55a)$$

$$z_{new2} = x_{new} \sin \theta + z_{new} \cos \theta \quad (55b)$$

The rotation operation will produce a change in the value in z_{new2} , differing from the original mesh grid z_{old} value of the hyperboloid surface. An example of a “mesh grid” is illustrated in Figure 3. It is a plotting grid system that provides a mesh to represent the shape of the hyperboloid. However, it is necessary to keep the original mesh grid z values after the hyperboloid is rotated so that further processing in conjunction with the other two hyperboloids can be carried out to locate the intersection point. That is, the z variable corresponds to the target altitude must be common to all three hyperboloids. In order to retain the original mesh grid z values of the hyperboloid associated with receiver-pair S1-S2; the left-hand-side of Equation (55b) is reset to the original mesh grid z value (i.e., $z_{new2} = z_{old}$); it is then solved together with the x-shifted hyperboloid equation in Equation (53),

$$z_{old} = x_{new'} \sin \theta + z_{new'} \cos \theta$$

$$x_{new'} = \frac{d}{2} \pm |a| \left(1 + \left(\frac{y_{new'}^2}{b^2} + \frac{z_{new'}^2}{b^2} \right) \right)^{1/2} \quad \text{at } y_{new'} = \text{constant} \quad (56)$$

The $(x_{new'}, z_{new'})$ values obtained from solving Equation (56) are then substituted into Equation (55a) for computing x_{new2} . This procedure is repeated for all $y_{new'} = y_{old}$ values to generate an x - z plane rotated hyperboloid. Note that the rotated hyperboloid will then have coordinates $(x, y, z) = (x_{new2}, y_{old}, z_{old})$, where y_{old} and z_{old} are the original hyperboloid mesh grid values.

The next step is to put the hyperboloid in the proper location with respect to the actual receivers S1 and S2 positions. This is done by shifting receiver S2 to $x = 0$ to act as a pivot for rotating about the z -axis. Thus the coordinates of S1, S2 and the x - z plane rotated hyperboloid will be translated to,

$$x_{new3} = x_{new2} - d \cos \theta$$

$$y_{new3} = y_{old}$$

$$z_{new3} = z_{old} \quad (57)$$

A rotation is then performed in the x - y plane about the z -axis in the clockwise direction by an angle,

$$\phi = \arctan \left(\frac{Y_1 - Y_2}{X_1 - X_2} \right) \quad (58)$$

After rotation, the coordinates of the hyperboloid are given by,

$$\begin{aligned}x_{new4} &= x_{new3} \cos(-\phi) - y_{new3} \sin(-\phi) \\y_{new4} &= x_{new3} \sin(-\phi) + y_{new3} \cos(-\phi) \\z_{new4} &= z_{old}\end{aligned}\tag{59}$$

The final placement of the ensemble is obtained by translating S2 to its ground truth location,

$$\begin{aligned}x_{final} &= x_{new4} + X_2 \\y_{final} &= x_{new4} + Y_2 \\z_{final} &= z_{old}\end{aligned}\tag{60}$$

The transforming procedures to the global coordinate frame for receiver-pairs S3-S4 and S1-S4 and their associated hyperboloids are the same as those in the coplanar case in Section 4.1.1 since the positions of receivers S1, S3 and S4 have not been changed in the non-coplanar set-up (see Table 6).

4.2.2 Non-coplanar target localization

Using this non-coplanar receiver configuration, target localization using the same Cramer-Rao Lower Bound error parameters, bandwidths $\beta = 1, 20$, and 300 MHz and system SNR $(S/N)_T = 16$ are examined. The target localization results are shown in Tables 12, 13, 14 respectively. Comparing to the respective results for the coplanar cases in Tables 9, 10, 11, it can be seen that there is a dramatic improvement in the accuracy of the target altitude z . This is especially evident in the large TDOA measurement error case ($\beta = 1$ MHz). The computed altitudes are much closer to the actual ground truth target altitude using the non-coplanar configuration (see Table 12); in contrast, the results for target altitude using the coplanar configuration are off significantly from the ground truth values (see Table 9). This clearly demonstrates the effect the non-coplanar receiver geometry has on the accuracy of the target localization process.

A quantitative explanation for the improvement of the target altitude estimate may be sought from Equation (9) of the algebraic approach model in Section 2.3. Essentially, the non-coplanar receiver S2 set-up can be seen as having one of the z variables non-zero in the 4x4 matrix of Equation (9), reverting the matrix to a full rank of 4. This restores a more stable condition in the matrix mathematically, permitting better accuracy in the estimate of the target altitude z .

Furthermore, it should also be noted that the accuracy of the computed target altitude is dependent on the height differential between the two receivers in the receiver-pair S1-S2. To demonstrate this, receiver S2 is raised higher to a height of $Z_2 = 500$ m, and the $\beta = 1$ MHz case is recomputed. The results are shown in Table 15. Comparing Table 15 with Table 12 (where receiver S2 is at a height $Z_2 = 200$ m), it is seen that the accuracy of the computed target altitude has improved notably with a higher Z_2 . By raising one of the receivers in the receiver-pair in height, this is equivalent to tilting the hyperboloid surface of receiver-pair S1-S2 to produce a

more pronounced intersection angle with the other two hyperboloid surfaces in the target localization process. Physically, it can be interpreted that when the height differential ($Z_i - Z_j$) in a receiver-pair is sufficiently large, it allows extraction of the target position in the z-direction more definitively. This physical explanation is corroborated by the relatively accurate target localization in the x and y directions, in which the receiver-pairs have large positions differentials; i.e. ($X_i - X_j$) and ($Y_i - Y_j$) are large, many hundreds of meters as shown in Table 6.

As an added note, the need for a non-coplanar receiver configuration is another reason why a minimum of four receivers are required in a TDOA system. It has already been mentioned in Section 2.1 that at least four receivers are needed to generate three independent TDOA measurements d_{ij} in order to process three-dimensional target localization. A fourth receiver in the system also ensures that a non-coplanar receiver geometry can be met. That is to say, a system with only three receivers will always be coplanar; the extra fourth receiver is needed to break the coplanar geometry.

4.3 Geometry-based target localization performance

To summarize briefly, a geometry-based approach to solving the set of TDOA equations (Equation (1)) is presented. The equations are solved for TDOA measurements that have varying amount of errors. There is a clear trend that as the TDOA error increases, the target localization accuracy degrades. A larger TDOA error induces a bigger deviation of the hyperboloid location from its ideal true position. Hence the intersection of three slightly displaced hyperboloids is shifted, resulting in an error in the target location.

The TDOA measurements with errors can be modelled using the standard deviation σ from CRLB as an error estimate; in particular, the signal bandwidth parameter β can be varied to provide varying outputs in the TDOA values. This approach covers a broad range of realistic scenarios where target transmission bandwidth can vary widely; they are reminiscent of typical drone detection scenarios. For example, drones transmit signals of different bandwidths depending on the tasks. For telemetry data uplink, the bandwidth used is around 3 MHz [32]. In the case of signal uplink such as surveillance video data, the bandwidth required is from 6 to 20 MHz (HD pictures and 4k videos) [34]. Over this range of bandwidth values β and a typical detection threshold $(S/N)_T = 16$, the model results indicate that fairly accurate target localization can be obtained from a passive system with four receivers in a non-coplanar geometry configuration.

Table 12: Comparisons of target localization from TDOA measurements with errors and actual target positions for non-coplanar receiver system. S2: $Z_2 = 200$ m, CRLB parametric values used: $\beta = 1$ MHz, $(S/N)_T = 12$ dB.

Time (time index)	Target ground truth [m]			Computed target location [m]		
	X_{Tg}	Y_{Tg}	Z_{Tg}	x	y	z
1	-660.00	9998.50	1000.00	-637.86	9837.28	400
2	-608.44	9328.48	1000.00	-624.27	9398.05	1700
3	-556.89	8658.46	1000.00	-543.75	8603.23	600
4	-505.33	7988.44	1000.00	-490.12	7938.34	800
5	-453.78	7318.42	1000.00	-441.23	7277.22	900

	Target ground truth [m]			Computed target location [m]		
Time (time index)	X_{Tg}	Y_{Tg}	Z_{Tg}	x	y	z
6	-402.22	6648.40	1000.00	-394.97	6562.24	900
7	-350.67	5978.38	1000.00	-344.75	5947.75	1200
8	-299.11	5308.36	1000.00	-288.28	5238.35	400
9	-247.56	4638.34	1000.00	-254.61	4595.83	1300
10	-196.00	3968.32	1000.00	-204.42	3923.01	1500

Table 13: Comparisons of target localization from TDOA measurements with errors and actual target positions for non-coplanar receiver system. S2: $Z_2 = 200$ m, CRLB parametric values used: $\beta = 20$ MHz, $(S/N)_T = 12$ dB.

	Target ground truth [m]			Computed target location [m]		
Time (time index)	X_{Tg}	Y_{Tg}	Z_{Tg}	x	y	z
1	-660.00	9998.50	1000.00	-658.36	9985.12	1000.00
2	-608.44	9328.48	1000.00	-607.37	9320.40	1000.00
3	-556.89	8658.46	1000.00	-556.09	8649.78	1000.00
4	-505.33	7988.44	1000.00	-504.86	7981.78	1000.00
5	-453.78	7318.42	1000.00	-452.51	7313.34	1000.00
6	-402.22	6648.40	1000.00	-401.72	6644.95	1000.00
7	-350.67	5978.38	1000.00	-349.92	5975.92	1000.00
8	-299.11	5308.36	1000.00	-298.84	5306.21	1000.00
9	-247.56	4638.34	1000.00	-247.41	4636.79	1000.00
10	-196.00	3968.32	1000.00	-195.37	3966.59	1000.00

Table 14: Comparisons of target localization from TDOA measurements with errors and actual target positions for non-coplanar receiver system. S2: $Z_2 = 200$ m, CRLB parametric values used: $\beta = 300$ MHz, $(S/N)_T = 12$ dB.

	Target ground truth [m]			Computed target location [m]		
Time (time index)	X_{Tg}	Y_{Tg}	Z_{Tg}	x	y	z
1	-660.00	9998.50	1000.00	-659.88	9997.62	1000.00
2	-608.44	9328.48	1000.00	-608.34	9327.81	1000.00
3	-556.89	8658.46	1000.00	-556.78	8657.86	1000.00
4	-505.33	7988.44	1000.00	-505.25	7987.87	1000.00
5	-453.78	7318.42	1000.00	-453.71	7317.98	1000.00
6	-402.22	6648.40	1000.00	-402.19	6648.08	1000.00
7	-350.67	5978.38	1000.00	-350.64	5978.16	1000.00
8	-299.11	5308.36	1000.00	-299.07	5308.13	1000.00
9	-247.56	4638.34	1000.00	-247.55	4638.23	1000.00
10	-196.00	3968.32	1000.00	-195.98	3968.19	1000.00

Table 15: Comparisons of target localization from TDOA measurements with errors and actual target positions for non-coplanar receiver system. S2: $Z_2 = 500$ m, CRLB parametric values used: $\beta = 1$ MHz, $(S/N)_T = 12$ dB.

Time (time index)	Target ground truth [m]			Computed target location [m]		
	X_{Tg}	Y_{Tg}	Z_{Tg}	x	y	z
1	-660.00	9998.50	1000.00	-644.08	9879.45	960
2	-608.44	9328.48	1000.00	-608.35	9296.76	910
3	-556.89	8658.46	1000.00	-548.58	8631.54	980
4	-505.33	7988.44	1000.00	-492.79	7952.89	1010
5	-453.78	7318.42	1000.00	-442.91	7285.06	1020
6	-402.22	6648.40	1000.00	-396.10	6566.37	980
7	-350.67	5978.38	1000.00	-342.35	5941.24	1040
8	-299.11	5308.36	1000.00	-290.40	5240.87	710
9	-247.56	4638.34	1000.00	-251.52	4600.34	1010
10	-196.00	3968.32	1000.00	-202.69	3933.65	1320

5 Multi-target detection and tracking

Small drones are becoming increasingly easier to access; it is therefore expected that encounters with multiple targets will become common occurrence. For practical counter-measures against drone surveillance applications, a detection system must be able to detect and track multiple targets simultaneously. Moreover, not only detection of multiple target is essential; the system must also be able to process the target information in real-time so that appropriate action can be taken immediately to address the threats.

5.1 A seven-target scenario case study

Using a seven-target scenario, a study is conducted to characterize the detection and localization of multiple targets. Figure 11 shows the trajectories of seven simultaneous targets moving inside the surveillance space of the passive detection system. The RF environment is sampled at ten time instants. The black circles in Figure 11 represent the ground truth positions (x,y) of the targets at the times when the target signals are being sampled by the receivers of the passive system; all seven targets are at an altitude of 1000 m. The sampled signals are then put through the cross-correlation process, producing a set of TDOA measurements for each of the three receiver-pairs of the passive system.

An illustration of multi-target TDOA measurements processed from receiver-pair (S1-S2) is shown in Figure 12. There are seven cross-correlation peaks, corresponding to the seven targets. The TDOA measurement value of each peak is given by its location along the range-difference axis as defined in Equation (46). As a note, it is assumed that each individual target is emitting independently and incoherently with respect to the one other; thus there is no cross-term interference between targets and hence is no spurious peaks in the cross-correlator output. This has been observed to be indeed the case in real experimental data of multiple emitter detection.

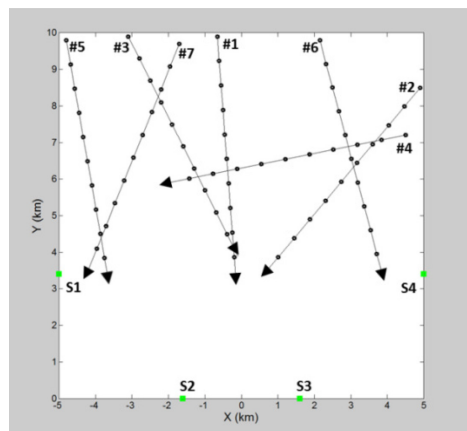


Figure 11: A seven-target scenario with multiple flight paths depicted in the monitored area; target positions at different time instants are given by the black circles and the positions of receivers S1, S2, S3, S4 are indicated by the green squares.

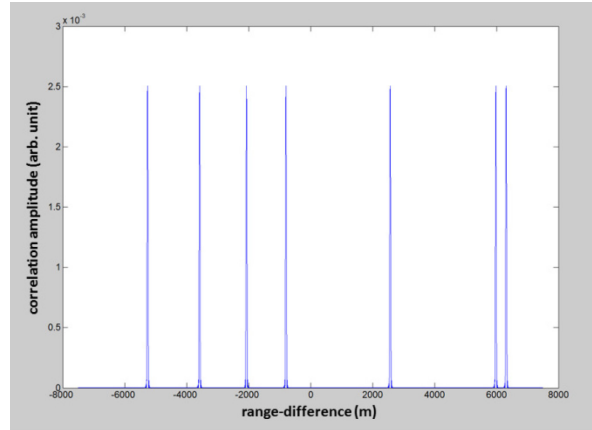


Figure 12: Cross-correlation outputs from a receiver-pair displaying seven detected target peaks as their corresponding TDOA measurement values along the range—difference axis.

The target locations are found by converting the three sets of multiple TDOA measurements from three receiver-pairs into intersecting hyperboloids as discussed in Section 2.3. In the case where there is only one target present, there is just one TDOA measurement recorded by each receiver-pair; thus the localization of a single target is straightforward as discussed in Section 4. In the case where there are multiple targets, there are multiple TDOA measurements made by each receiver-pair as seen in Figure 12. A permutation of all possible combinations from the three sets TDOA measurements recorded by the three receiver-pairs has to be carried out to find all the targets. The total number of combinations that has to be searched is n^3 , where n is the number of targets detected by each receiver-pair.

In the seven-target scenario, there will be $7^3 = 343$ sets of possible combinations of three TDOA measurement values. Among this large number of combinations, there are only seven combinations that correspond to the actual target locations. The correct combinations in the permutation are found by using the TDOA measurements from receiver-pair (S1-S2) as the reference set. Each TDOA measurement in this reference set is then combined with all the TDOA measurements from receiver-pairs (S3-S4) and (S1-S4). The combination that produces a minimum S in Equation (51) from the intersection of three hyperboloids determines the target location. This procedure is repeated for all TDOA values in the reference set to compute the target locations of the seven targets.

To give a clearer picture of the search procedure for all combinations in multi-target localization described above, a simpler two-target case is presented in Table 16 as an illustrative example. The cross-correlator output from receiver-pair (S1-S2) produces two TDOA values, A and D , corresponding to two detected targets. Similarly, TDOA values B and E are generated from receiver-pair S3-S4, and TDOA values C and F are produced from receiver-pair S1-S4 respectively. Thus, a total of $2^3 = 8$ sets of possible TDOA combinations among the three receiver-pairs are generated (see lower part of Table 16). It is obvious that only the sets (A,B,C) and (D,E,F) are the correct sets that can ideally produce intersecting hyperboloids with a minimum S value in Equation (51) in the permutation to pinpoint the two target locations.

Table 16: A permutation of all possible combinations of the TDOA values for a 2-target scenario.

	Target #1	Target #2
Receiver-pair (S1-S2)	A	D
Receiver-pair (S3-S4)	B	E
Receiver-pair (S1-S4)	C	F
Permutation of TDOA values in generating all possible TDOA combinations from two targets		
ABC, ABF, AEC, AEF, DBC, DBF, DEC, DEF		

5.2 Multi-target localization

To characterize the multi-target localization process, the non-coplanar receiver configuration is used since it provides more accurate target altitude estimate as discussed in Section 4.2.2; hence it offers a better system configuration for evaluating the localization performance. The non-coplanar receiver set-up is the same one used in Section 4.2 with receiver S2 at $Z_2 = 200$ m above the ground (see also Table 6). CRLB parametric values of $\beta = 20$ MHz, and a $(S/N)_T = 12$ dB (or 16) are used in the cross-correlation process to compute the TDOA measurements with errors included. These TDOA values are then applied to the procedure described in Section 5.1 to find the locations of the seven targets at various time instants. Results of the computed multi-target positions (x,y) are shown in Figure 13 and the corresponding target altitudes (z) are tabulated in Table 17. An altitude scan with increment $\Delta z = 100$ m is used to speed up the search of a large number of TDOA combinations that has to be searched in finding the intersection. First, it can be seen from Figure 13 that there are few instances when the computed target positions (red diamonds) are incorrectly placed with respect to the actual target ground truths (black open circles). These erroneous locations are indicated in Figure 13 by the arrows, pointing to the corresponding actual ground truths.

These target location errors are analyzed, and the problems are traced to two possible sources. One source of the location error may be due to TDOA measurement errors in d_{ij} . The second source of location error may be due to the TDOA permutation combinations used in computing the target localization output. The four smaller errors in Figure 13 may be caused simply by the first source, TDOA measurement errors. Errors in d_{ij} can cause the hyperboloid positions to be shifted slightly, resulted in placing the intersection of the three hyperboloids at a different location. The large location error seen in Figure 13 (bottom right) may be due to the second source. In searching through different combinations in the permutations, there may be instances in which a particular combination of three hyperboloids might contain a hyperboloid that is belonging to a different target. This combination produces a minimum S in the computation of Equation (51), and hence leads to an error in the localization. Such occurrence is also a consequence of TDOA measurement errors. With larger errors in the TDOA measurement values, it could become more probable that a combination of hyperboloids belonging to different targets in the permutation may produce an intersection with a minimum S value. As a result, the computed target location will be off considerably for the intended target as seen in Figure 13.

To verify that TDOA measurement errors can affect multi-target localization accuracy, the size of the TDOA measurement error is reduced by increasing the SNR of the TDOA signal. The target localization computation is rerun using a SNR value $(S/N)_T = 32$ dB, and a bandwidth $\beta = 20$ MHz. An increase in $(S/N)_T$ from 12 dB to 32 dB corresponds to a reduction in the TDOA measurement

error by a factor of ten according to Equations (44) and (45). Figure 14 and Table 18 show the outputs of the target positions (x,y) and target altitudes (z) respectively. It is seen that all the computed target positions are placed correctly and at the correct target altitude. These results indicate that by reducing the TDOA measurement errors, multiple targets can be located accurately.

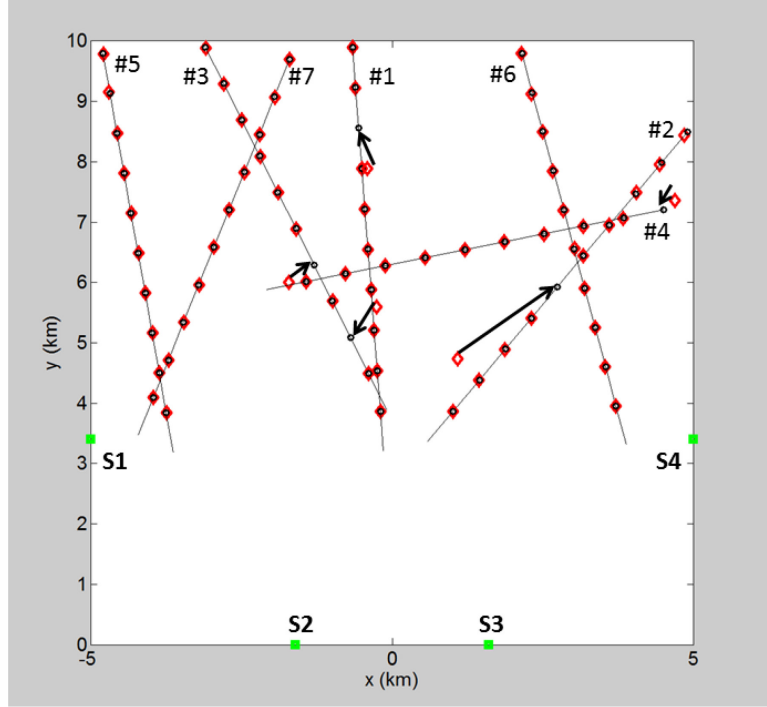


Figure 13: Computed target locations (x,y) from a non-coplanar configuration.
 $S2: Z_2 = 200 \text{ m}$; CRLB parametric values used: $\beta = 20 \text{ MHz}$, $(S/N)_T = 12 \text{ dB}$.

Table 17: Computed target altitudes from a non-coplanar configuration. $S2: Z_2 = 200 \text{ m}$. CRLB parametric values used: $\beta = 20 \text{ MHz}$, $(S/N)_T = 12 \text{ dB}$. Actual target altitude = 1000 m .

time	target altitude (m)						
	T#5	T#3	T#7	T#1	T#6	T#2	T#4
1	1000.00	1000.00	1000.00	1000.00	1000.00	800.00	1600.00
2	1100.00	1000.00	1000.00	1000.00	900.00	900.00	1000.00
3	1000.00	1000.00	1000.00	700.00	1000.00	1000.00	1100.00
4	1000.00	1000.00	1000.00	1000.00	1000.00	1000.00	1000.00
5	1000.00	1000.00	1000.00	1000.00	1000.00	1000.00	1000.00
6	1000.00	1000.00	1000.00	1000.00	1000.00	1100.00	1700.00
7	1000.00	1000.00	600.00	1000.00	1000.00	1000.00	1000.00
8	1000.00	1000.00	1000.00	1000.00	1000.00	1000.00	1000.00
9	1000.00	1000.00	1000.00	800.00	1000.00	1000.00	1000.00
10	1000.00	1000.00	1000.00	1000.00	1000.00	1000.00	1000.00

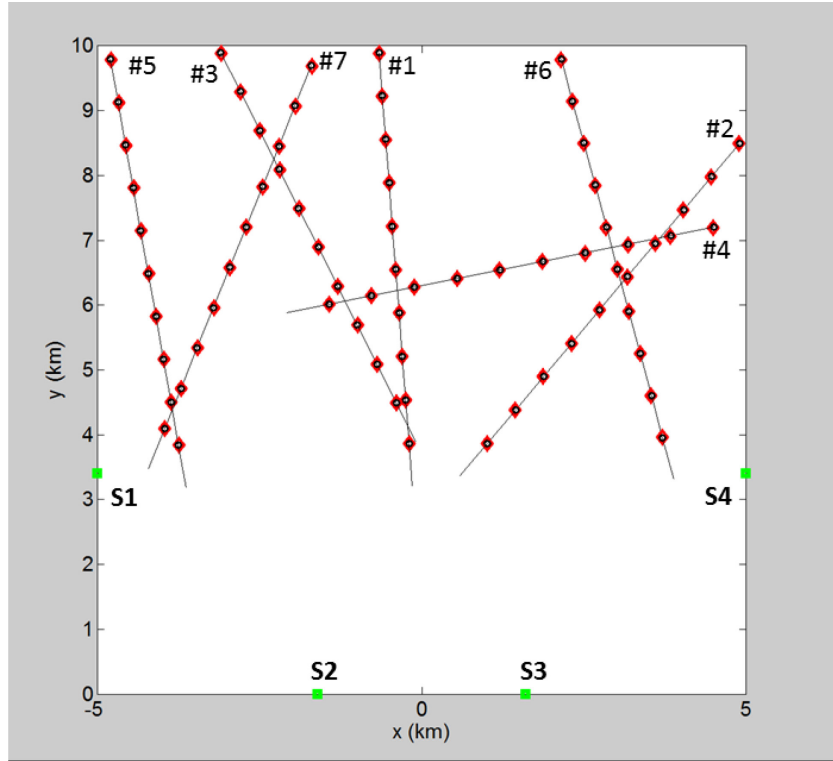


Figure 14: Computed target locations (x,y) from a non-coplanar configuration. S2: $Z_2 = 200$ m, CRLB parametric values used: $\beta = 20$ MHz, $(S/N)_T = 32$ dB.

Table 18: Computed target altitudes from a non-coplanar receiver configuration. S2: $Z_2 = 200$ m, CRLB parametric values used: $\beta = 20$ MHz, $(S/N)_T = 32$ dB. Actual target altitude = 1000 m.

	target altitude (m)						
	T#5	T#3	T#7	T#1	T#6	T#2	T#4
time							
1	1000.00	1000.00	1000.00	1000.00	1000.00	1000.00	1000.00
2	1000.00	1000.00	1000.00	1000.00	1000.00	1000.00	1000.00
3	1000.00	1000.00	1000.00	1000.00	1000.00	1000.00	1000.00
4	1000.00	1000.00	1000.00	1000.00	1000.00	1000.00	1000.00
5	1000.00	1000.00	1000.00	1000.00	1000.00	1000.00	1000.00
6	1000.00	1000.00	1000.00	1000.00	1000.00	1000.00	1000.00
7	1000.00	1000.00	1000.00	1000.00	1000.00	1000.00	1000.00
8	1000.00	1000.00	1000.00	1000.00	1000.00	1000.00	1000.00
9	1000.00	1000.00	1000.00	1000.00	1000.00	1000.00	1000.00
10	1000.00	1000.00	1000.00	1000.00	1000.00	1000.00	1000.00

5.2.1 Target localization using coplanar receiver configuration

It would also be insightful to compare the difference in the target localization accuracy between a non-coplanar receiver system and a coplanar receiver system in a multi-target scenario. The

four-receiver coplanar and non-coplanar systems given in Table 6 are compared in their target localization performance. The Cramer-Rao Lower Bound parameters, β and $(S/N)_T$ used in the coplanar configuration are the same as those for the non-coplanar case. Setting $\beta = 20$ MHz and $(S/N)_T = 12$ dB, Figure 15 shows the computed results of multi-target track positions (x,y) from coplanar configuration. The results show that very accurate target track positions in (x,y) can be obtained; in fact, they are somewhat better than the non-coplanar configuration case (see Figure 13). However, the accuracy in the target altitudes are off considerably; this is shown in Table 19. They are notably worse than those in Table 17 for the non-coplanar configuration. Explanation for the poor computed results in the target altitude for the coplanar configuration is given in Section 4.1.3. These results are consistent with the results of the single target case from a coplanar system configuration as seen in Table 10.

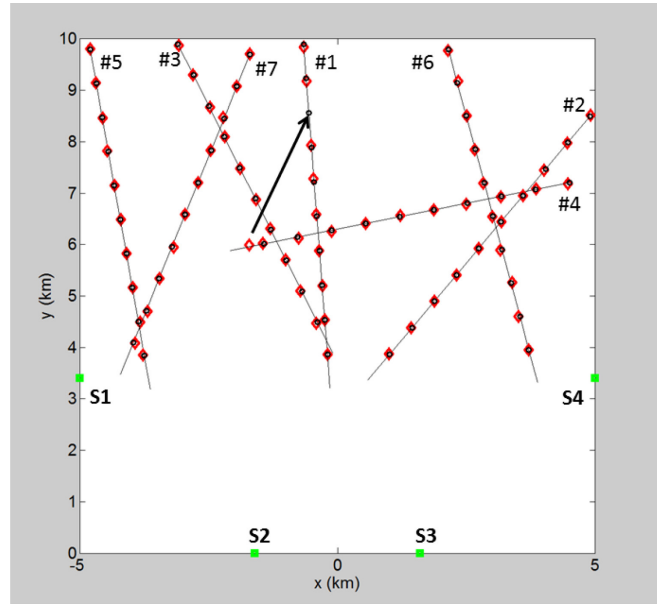


Figure 15: Computed target locations from a coplanar receiver configuration. S2: $Z_2 = 0$ m, CRLB parametric values used: $\beta = 20$ MHz, $(S/N)_T = 12$ dB.

Table 19: Computed target altitudes from a coplanar configuration. S2: $Z_2 = 0$ m, CRLB parametric values used: $\beta = 20$ MHz, $(S/N)_T = 12$ dB. Actual target altitude = 1000 m.

time	target altitude (m)						
	T#5	T#3	T#7	T#1	T#6	T#2	T#4
1	1100.00	900.00	1100.00	400.00	900.00	1100.00	900.00
2	1100.00	1100.00	1100.00	300.00	1300.00	1000.00	1100.00
3	1000.00	800.00	1200.00	600.00	1100.00	1000.00	900.00
4	1100.00	1100.00	1000.00	1500.00	1000.00	800.00	1000.00
5	1000.00	1000.00	900.00	1800.00	1100.00	900.00	1100.00
6	1000.00	1000.00	700.00	1600.00	1400.00	900.00	1000.00
7	1000.00	800.00	1300.00	1200.00	1100.00	1000.00	800.00
8	1000.00	1000.00	1500.00	0	0	1100.00	1100.00
9	900.00	900.00	0	1900.00	1100.00	800.00	900.00
10	900.00	1100.00	1300.00	1900.00	1000.00	800.00	1000.00

The TDOA measurement error is then reduced by increasing the SNR value to $(S/N)_T = 32$ dB from 12 dB, the multi-target scenario is recomputed. The computed target positions (x,y) are shown in Figure 16, and the target altitude results are given in Table 20. Comparing Figure 15 and Figure 16, the results are almost identical, even though the latter has a smaller TDOA measurement error. However, comparing Table 19 and Table 20, it is seen that there is a notable improvement in the altitude accuracy. Thus, these results re-affirm that a reduction in the TDOA measurement error can improve the overall accuracy in the target localization as seen in the single-target case in Section 4.1.3. But these are still not as good as the results using the non-coplanar receiver configuration shown in Figure 14 and Table 18, which show that target localizations are accurately computed. These comparative results further demonstrate that the non-coplanar configuration offers better target localization accuracy.

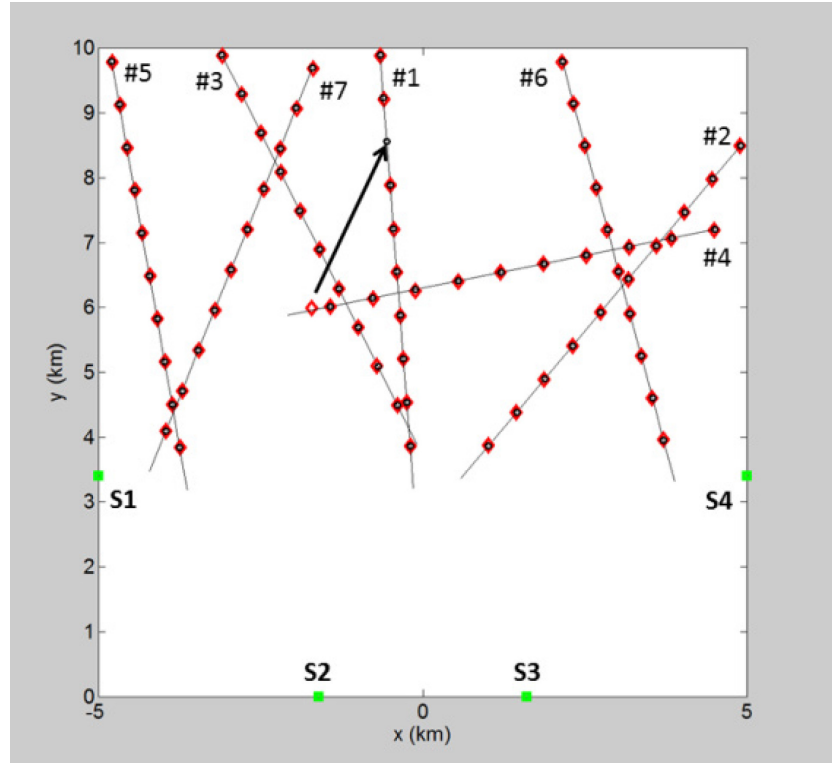


Figure 16: Computed target locations from a coplanar receiver configuration. S2: $Z_2 = 0$ m, CRLB parametric values used: $\beta = 20$ MHz, $(S/N)_T = 32$ dB.

Table 20: Computed target altitudes from a coplanar receiver configuration. S2: $Z_2 = 0$ m, CRLB parametric values used: $\beta = 20$ MHz, $(S/N)_T = 32$ dB. Actual target altitude = 1000 m.

time	target altitude (m)						
	T#5	T#3	T#7	T#1	T#6	T#2	T#4
1	1000.00	1000.00	1000.00	1000.00	1000.00	1000.00	1000.00
2	1000.00	1000.00	1000.00	900.00	1000.00	1000.00	1000.00
3	1000.00	1000.00	1000.00	500.00	1000.00	1000.00	1000.00
4	1000.00	1000.00	1000.00	1000.00	1000.00	1000.00	1000.00
5	1000.00	1000.00	1000.00	900.00	1000.00	1000.00	1000.00
6	1000.00	1000.00	1000.00	900.00	1000.00	1000.00	1000.00
7	1000.00	1000.00	1000.00	900.00	900.00	1000.00	1000.00
8	1000.00	1000.00	1100.00	0	1400.00	1000.00	1000.00
9	1000.00	1000.00	800.00	1700.00	1200.00	900.00	1000.00
10	1000.00	1000.00	900.00	1100.00	1000.00	900.00	1000.00

5.2.2 Effect of receiver-pair tilt in non-coplanar configuration

For completeness, the amount of tilt given to a receiver-pair in the non-coplanar configuration is also investigated to assess its effect in the target localization performance. As illustrated graphically in Figure 8, the target location (x,y,z) is determined from the intersection of three hyperboloid surfaces. In the coplanar receiver configuration case, all three hyperboloid surfaces are oriented symmetrically about the x - y plane; this can result in an ambiguous intersection location, forming a line-like intersection from the three surfaces as seen in Figure 8. However, if one of the receiver-pairs is tilted out of the common plane shared by the other two receiver-pairs, the hyperboloid surface that corresponds to the tilted receiver-pair would become asymmetric with respect to the x - y plane; i.e., tilting at a greater angle with respect to the x - y plane. This tilted hyperboloid would intersect with the other two intersecting hyperboloid surfaces to form a more definitive intersecting point. Quantitatively, the height differential $(Z_2 - Z_1)$ of the tilted receiver-pair as discussed in Section 4.2.2 is bigger when the receiver-pair tilt angle is larger; hence, this leads to better z accuracy.

To examine the effect of an increase in the tilt angle of a receiver-pair has on the target localization, receiver S2 of the receiver-pair S1-S2 is raised to a height $Z_2 = 400$ m from 200 m. The target-tracks positions (x,y) for a larger tilt in the receiver-pair S1-S2 are shown in Figure 17. The computed target positions are quite accurate; only one target position point is computed incorrectly (target T#4). In comparison, Figure 13 have 5 target position points that are off from the ground truth positions when receiver S2 is at a lower height, $Z_2 = 200$ m. More notably, the target altitude is computed correctly at the actual target altitude of 1000 m using the larger tilt, except one single point for target T#4; this is shown in Table 21. These results are much better than those in Table 17 with a smaller tilt ($Z_2 = 200$ m).

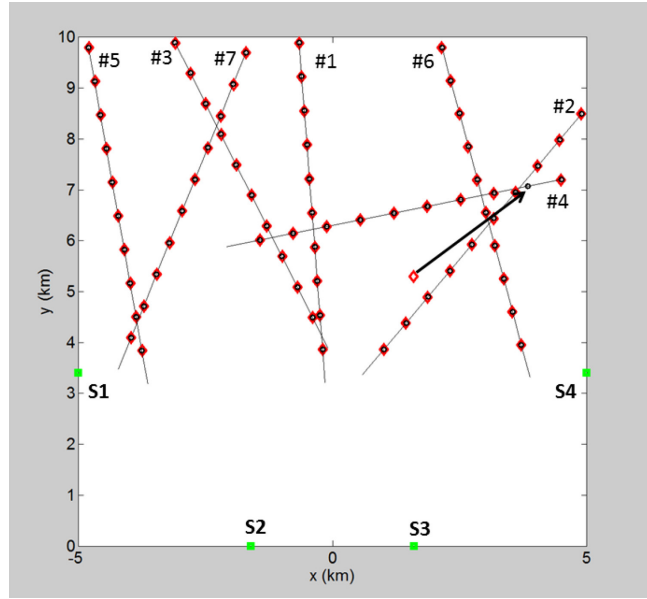


Figure 17: Computed target locations from a no-coplanar receiver configuration S2: $Z_2 = 400$ m, CRLB parametric values used: $\beta = 20$ MHz, $(S/N)_T = 12$ dB.

Table 21: Computed target altitudes from a non-coplanar receiver configuration. S2: $Z_2 = 400$ m, CRLB parametric values used: $\beta = 20$ MHz, $(S/N)_T = 12$ dB. Actual target altitude = 1000 m.

time	target altitude (m)						
	T#5	T#3	T#7	T#1	T#6	T#2	T#4
1	1000.00	1000.00	1000.00	1000.00	1000.00	1000.00	1000.00
2	1000.00	1000.00	1000.00	1000.00	1000.00	1000.00	400.00
3	1000.00	1000.00	1000.00	1000.00	1000.00	1000.00	1000.00
4	1000.00	1000.00	1000.00	1000.00	1000.00	1000.00	1000.00
5	1000.00	1000.00	1000.00	1000.00	1000.00	1000.00	1000.00
6	1000.00	1000.00	1000.00	1000.00	1000.00	1000.00	1000.00
7	1000.00	1000.00	1000.00	1000.00	1000.00	1000.00	1000.00
8	1000.00	1000.00	1000.00	1000.00	1000.00	1000.00	1000.00
9	1000.00	1000.00	1000.00	1000.00	1000.00	1000.00	1000.00
10	1000.00	1000.00	1000.00	1000.00	1000.00	1000.00	1000.00

5.3 Overlapping TDOA measurements

So far in the seven-target scenario, all seven targets are detected in the cross-correlation process. However, as more targets are entering the surveillance area, it is conceivable that the TDOA measurements from two individual targets can have the same TDOA value; thus there might only be $(n-1)$ targets detected from n targets that are actually present. In other words, a receiver-pair could generate the same TDOA measurement value for two different targets even though the two targets can be at different locations. In general, more than two targets can have the same TDOA value.

To investigate the overlapping TDOA measurement problem, three more targets are added to the seven-target scenario in Figure 11. Figure 18 shows the ground truth positions of ten targets at ten time instants. With ten simultaneous targets present, there are a number of occurrences in which only nine TDOA measurements are detected by the cross-correlation process. Overlapping occurs when the profile H in Equation (35) between two targets are separated less than two resolution bins; i.e., $2\Delta r = 2c/\beta$ in Equation (43). Table 22 shows the occurrences of these overlapping TDOA measurements, producing only nine TDOA measurement values at a number of time instants; at all other times, ten TDOA peaks are obtained. These occur in all three receiver-pairs of the receiver system. The overlapped TDOA measurements are identified by the red boxes. The receiver set-up (non-coplanar) and system parameters used are the same as those for the seven-target case in Figure 14.

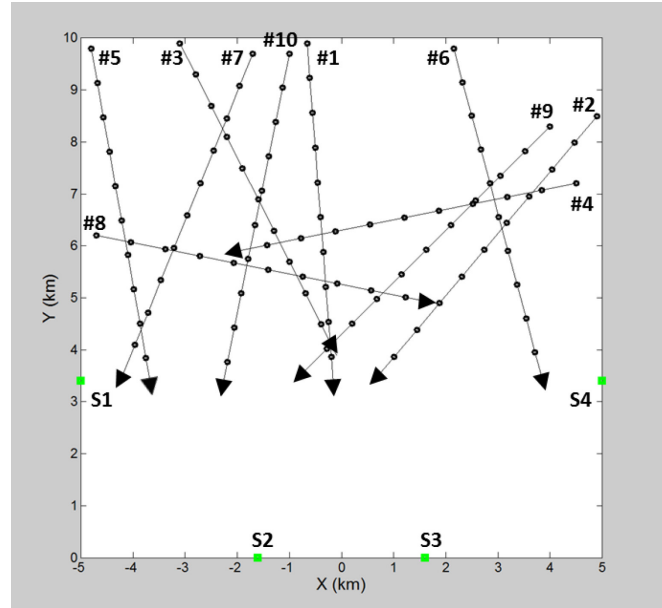


Figure 18: Flight paths for a ten-target scenario; target positions at ten time instants are given by the small open circles.

Table 22: Occurrence of overlapping TDOA measurements in a ten-target scenario, resulted in only nine TDOA values at time instant t . S2: $Z_2 = 200$ m, CRLB parametric values used: $\beta = 20$ MHz, $(S/N)_T = 32$ dB.

TDOA measurements from Receiver-pair (S1-S2)									
t=4	-3792.90	-2708.85	-2594.55	-2502.60	-2047.80	-1572.00	-47.55	315.45	639.30
t=7	-3612.00	-2943.30	-1702.65	-1542.45	-710.70	-418.50	402.45	922.20	978.60
TDOA measurements from Receiver-pair (S3-S4)									
t=5	-762.15	-659.40	-199.35	242.40	837.90	2107.20	2201.70	2891.55	3014.55
t=7	-1257.15	-933.75	-507.90	-187.05	-0.45	292.20	1090.95	2038.50	2948.40
TDOA measurements from Receiver-pair (S1-S4)									
t=6	-6424.95	-4715.10	-2767.80	2523.90	-669.75	1994.10	2821.65	4663.20	4816.05

The targets involved in the overlapped TDOA values are identified and shown in Table 23. The TDOA values of the individual targets if they were the only target present individually are also shown in Table 23. The cross-correlator is not able to resolve the two closely spaced TDOA peaks distinctly; the resolution spacing of the cross-correlator output is given by $\Delta r = c/\beta = 15$ m in Section 3.3.1. However, two peaks separated by a range-difference of 15 m apart do not give definitively two separate peaks as outputs. In order to have two distinct peaks as outputs from the cross-correlator, the peak location procedure is set such that two adjacent target peaks must be at least $2\Delta r = 30$ m apart; otherwise, the two TDOA peaks are merged as one single peak in the output. This is seen in the results shown in Table 23. For example, in the $t = 6$ case, two targets (T#3 and T#8) are 28 m apart in range difference; but they are output as one overlapped peak.

Table 23: TDOA measurement values of individual targets and overlapped
TDOA measurement values between two targets. S2: $Z_2 = 200$ m,
CRLB parametric values used: $\beta = 20$ MHz, $(S/N)_T = 32$ dB.

TDOA measurements from receiver-pair (S1-S2)	
t=4:	TDOA from individual target: 320.40 (T#4); 310.50 (T#9) Overlapped TDOA: 315.45 (T#4 & T#9)
t=7:	TDOA from individual target: -698.85 (T#1); -722.55 (T#8) Overlapped TDOA: -710.70 (T#1 & T#8)
TDOA measurements from receiver-pair (S3-S4)	
t=5:	TDOA from individual target: 247.95 (T#3); 236.85 (T#10) Overlapped TDOA: 242.40 (T#3 & T#10)
t=7:	TDOA from individual target: 1102.05 (T#4); 1079.70 (T#9) Overlapped TDOA: 1090.95 (T#4 & T#9)
TDOA measurements from receiver-pair (S1-S4)	
t=6:	TDOA from individual target: -2546.70 (T#3); -2518.65 (T#8) Overlapped TDOA: -2523.90 (T#3 & T#8)

5.3.1 Analysis of target localization with overlapping TDOA values

Computed results of target positions (x,y) for the ten-target scenario are shown in Figure 19. There are a number of locations with no computed target where they are supposed to be; these occur for targets T#1, T#2, T#6 and T#9 (i.e., missing red diamonds). The problematic target locations are marked by black square boxes in Figure 19.

An analysis is carried out to examine these missing target locations and how they can be accounted for. For the two missing computed target locations for targets T#1 and T#4, they occur at time $t = 4$ and 7. Their absence can be traced to the overlapped TDOA measurement values detected by receiver-pair (S1-S2). At $t = 4$, target T#4 shares a TDOA value with T#9, and at $t = 7$, target T#1 shares a TDOA value with T#8. This is shown in Table 23.

In the computation procedure that converts the TDOA measurements into target localization, receiver-pair S1-S2 is used as the reference in the cross-correlator to determine the number of TDOA values detected at a given time instant t (see Section 5.1). At $t = 4$ and 7, there are only nine TDOA measurement values detected by receiver-pair S1-S2 as indicated in Table 22. Therefore, it is expected that there would be a target missing in the computed target track at each

of these two time instants. Since the target locations for T#9 at $t = 4$ and T#8 at $t = 7$ are computed as shown in Figure 19, TDOA information on T#1 and T#4 is assumed to be lost due to the overlapping. Hence, no computed target is available for T#1 at $t = 7$ and T#4 at $t = 4$. This is indeed seen in Figure 19 for targets T#1 and T#4 in which there is no computed targets (red diamonds) at the actual target locations (black square boxes).

There are two other unfilled target locations in the tracks for targets T#2 and T#6 as seen in Figure 19 (black square boxes). There are also two computed target locations (circled red diamonds) that are erroneously located away from any of the target tracks. Detailed tracing of the computational results indicate that the computed location of T#2 at $t = 4$ is in error, and the location of T#6 at $t = 7$ is in error. These incorrectly computed target locations and their true locations are linked by the arrows in Figure 19. The location errors are attributed to the permuted TDOA combination sequence in which not all three hyperboloids are belonging to the same target, but the sequence is producing a minimum S value at the intersection as discussed in Section 5.2.

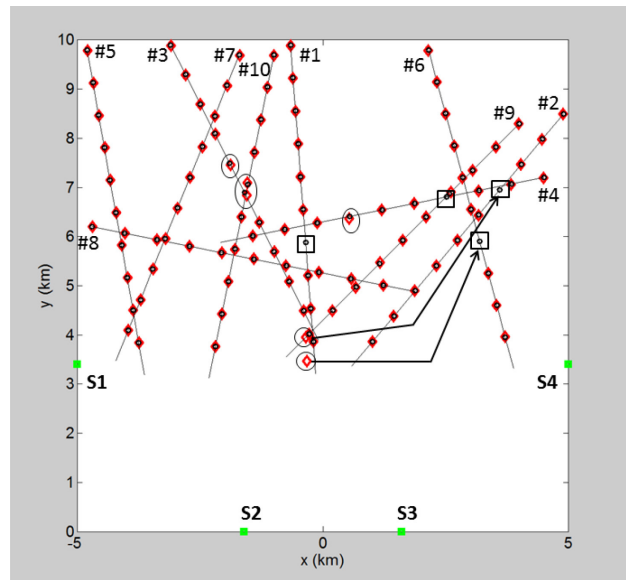


Figure 19: Computed target locations (x,y) from TDOA measurements with overlapping values. S2: $Z_2 = 200$ m (non-coplanar), CRLB parametric values used: $\beta = 20$ MHz, $(S/N)_T = 32$ dB.

Table 24: Target altitudes computed from TDOA measurements with overlapped values. Actual target altitude = 1000 m.

time	target_altitude (m)		T#3	T#7	T#10	T#1	T#6	T#9	T#2	T#4
	T#8	T#5								
1	1000.00	1000.00	1000.00	1000.00	1000.00	1000.00	1000.00	1000.00	1000.00	1000.00
2	1000.00	1000.00	1000.00	1000.00	1000.00	1000.00	1000.00	1000.00	1000.00	1000.00
3	1000.00	1000.00	1000.00	1000.00	1000.00	1000.00	1000.00	1000.00	1000.00	1000.00
4	1000.00	1000.00	1000.00	1000.00	1000.00	1000.00	1000.00	1300.00	1900.00	
5	1000.00	1000.00	800.00	1200.00	1000.00	1000.00	1000.00	1000.00		1000.00
6	1000.00	1000.00	400.00	1000.00	1100.00	1000.00	1000.00	1000.00	1000.00	1000.00
7	1000.00	1000.00	1000.00	1000.00	1300.00		600.00	1300.00	1000.00	1900.00
8	1000.00	1000.00	1000.00	1000.00	1000.00	1000.00	1000.00	1000.00	1000.00	1000.00
9	1000.00	1000.00	1000.00	1000.00	1000.00	1000.00	1000.00	1000.00	1000.00	1000.00
10	1000.00	1000.00	1000.00	1000.00	1000.00	1000.00	1000.00	1000.00	1000.00	1000.00

As indicated in Table 23, there are also overlapped TDOA measurement values at $t = 5, 6, 7$ from receiver-pairs S3-S4 and S1-S4, involving targets T#3, T#4, T#8, T#9 and T#10. Since these overlaps are not occurring in the reference receiver-pair, the overlapped TDOA values are reused in the permutation of the TDOA combinations; thus there would not be any missed target detections at these times. But because the overlapped TDOA values are very close to the TDOA values of the individual targets, the error introduced to the target localization computation would be small. This is, in fact, corroborated in the computed results in Figure 19. Some of the computed target locations have small but noticeable deviations in the computed target locations (red diamonds) from the actual locations (black circles) where TDOA overlaps occur at $t = 5, 6$, and 7 . These are highlighted by the black ovals for targets T#3, T#4 and T#10 in Figure 19. For completeness, the computed target altitudes for the ten targets at various times are shown in Table 24. It can be seen that the occurrences of TDOA overlaps also degrade the accuracy of some of the computed target altitudes quite notably.

5.4 Approach to real-time multi-target processing

For practical applications, a target detection system must have a capability to provide location information of multiple targets in real time so that the intruding targets can be dealt with immediately. One advantage of the geometric approach is that it may be able to facilitate real-time processing, especially in multi-target scenarios. Using the geometric approach, each of the three TDOA equations in Equation (1) can be solved individually; a hyperboloid that corresponds to a given TDOA measurement value d_{ij} can be pre-computed. Look-up tables for a set of hyperboloids corresponding to a range of d_{ij} values can be generated. The look-up tables can speed up the target localization computing process, thus helping to facilitate real-time multiple targets processing.

For a given receiver system configuration, the receiver locations are a-priori information. Based on the separation distance d between a pair of receivers (i, j), the range of the TDOA measurement values d_{ij} is between $-d < d_{ij} < d$ according to Equation (3). Furthermore, based on a given operating receiver bandwidth and detection SNR, the spacing of the d_{ij} values needed in generating the look-up tables can be determined from the Cramer-Rao Lower Bound error given in Equation (43).

Using a receiver system configured as shown in Figure 1, and the receiver locations given in Table 6 as an example, a description on how a set of TDOA values can be determined for generating look-up tables of hyperboloids is given as follows. For receiver-pair S1-S2, the separation distance between receivers S1 and S2 is $d = 4812$ m (non-coplanar case) from Table 6. For receiver operating with a bandwidth of 20 MHz, and a detection SNR $(S/N)_T = 16$, the set of TDOA values d_{12} will have a spacing of $\epsilon = 1.5$ m as given by Equation (43). Thus a set of 6417 d_{12} values $(2d/\epsilon + 1)$ are required in the look-up table for receiver-pair (S1-S2); i.e., $d_{12} = 0, \pm 1.5, \pm 3, \dots, \pm 4812$. Similarly, it will require 6417 d_{34} TDOA values for receiver-pair S3-S4. For receiver-pair S1-S4, the distance separating S1 and S4 is $d = 10000$ m; therefore, $2d/\epsilon + 1 = 13334$ d_{14} TDOA values are required. A hyperboloid can be pre-computed for each of these TDOA values, totaling 26168 in all.

With the advent in efficient file indexing and file search algorithms, pertinent hyperboloid data corresponding to specific d_{ij} TDOA values can be retrieved quickly from look-up tables.

Furthermore, for a n -target scenario, there are n^3 combinations of three-hyperboloids from a permutation of n targets that have to be search to find the n -target localization. Since the n^3 permutation is intrinsically parallel in structure as seen in the two-target permutation example in Table 16, processing of n^3 combinations using parallel-computing can facilitate real-time target localization to be realized for a reasonable size n . More quantitative investigation on parallel processing of multi-target localization using pre-computed look-up tables for the hyperboloids will be needed.

Table 25 gives an indication of the amount of computing time used in processing TDOA measurements conducted in this study. The time taken includes the generation and orientation of the three hyperboloids as outlined in Section 4, and the search for minimum S in Equation (51) for n targets in a sequential permutation processing for each target. The computations are performed in a Dell T7400 workstation.

Table 25: *Computation time consumed in target localization processing for different number of targets detected using sequential processing.*

n (no. of targets detected)	t (coplanar configuration)	t (non-coplanar configuration)
1	0.4 s	18.6 s
3	2.8	56.1
7	30.8	147.1
10	89.5	236.0

It can be seen from Table 25 that in order to attain real-time processing, especially in the non-coplanar receiver configuration, pre-computing of the hyperboloids in their proper orientations and parallel processing of multiple targets will be necessary. The geometric approach can accommodate pre-computing of the hyperboloids, hence saving considerable processing time.

The longer computing time required for the non-coplanar configuration is due to resampling of the mesh of the hyperboloid in the z -direction so that all three hyperboloids have the same z -grid mesh to determine the target localization properly; see Section 4.2.1. However, computing time requirement should no longer be an issue if the hyperboloids are pre-computed. Using look-up tables, efficient data-file search algorithms, parallel processing, faster multi-processor computer, and further streamlining and optimizing of the computational codes, it is conceivable that a target localization processing time under one second can be attained for a ten-target scenario, even for a non-coplanar system configuration.

It should be noted that pre-computing will not be feasible in the algebraic approach. Solving Equation (1) by numerical iterative methods requires a set of three TDOA measurement values together. The permutation of all possible combinations of a set of three TDOA values is simply too overwhelming, about $6417 \times 6417 \times 13334 \approx 5 \times 10^{11}$ combinations. The algebraic approach will also potentially run into issues on how to handle convergence in the iterative numerical procedure when processing “non-target” d_{ij} combinations in multi-target cases; i.e., not all d_{ij} from the same target. This will require more complex algorithmic procedures and will use up more computing time, making real-time processing difficult to attain with the algebraic approach. On a positive note, the pre-computed outputs are the solutions to the possible target locations; in other words, a look-up solution table to Equation (1) is generated.

6 Conclusions

Passive target localization exploiting the target's emitting radio-frequency signals has been investigated. The TODA method is employed in the passive target localization process. A geometry-based approach to solving the TDOA problem has been proposed. TDOA measurements are first converted to three-dimensional hyperboloid surfaces to represent the possible target locations. The actual target location is then determined by searching for the intersection of the hyperboloid surfaces. Target location accuracy is examined as a function of TDOA measurement errors. The errors are modelled using the Cramer-Rao Lower Bound to provide an estimate on how accurate the TDOA measurements can be made in the signal correlation process.

Numerical results from the analysis show that TDOA measurement errors affect target location accuracy as expected, but they affect the target's altitude more acutely. It is shown that more accurate target localization can be achieved when non-coplanar receiver system configuration is employed. A mathematical explanation and a physical interpretation have been given to explain the receiver system configuration effect on the target localization accuracy.

Localization of multiple targets using the geometry-based approach has also been examined. Results indicate that accurate multiple target localization (up to ten targets simultaneously) can be obtained; however, real-time processing may be a challenge. The geometric approach may offer a solution to reduce a significant portion of the processing time. It can be used in conjunction with pre-computed look-up tables for target hyperboloids to improve the processing speed. This opens up a potential means to real-time multi-target localization processing.

As drones become more affordable and accessible, multi-target threats are likely to become more likely to occur. A multi-target, real-time detection and tracking will likely be a desirable capability, and may become a standard requirement in a field system to handle practical drone counter-measures applications. This report has proposed and examined an approach that could achieve such capability realistically with current data storage and processing technologies.

References

- [1] R.A. Poisel, “Electronic Warfare Target location Methods”, ArtTech House, Boston, 2005.
- [2] D. Munoz, F. Bouchereau, C. Vargas, and R. Enriquez-Caldera, “Position Location Techniques and Applications”, Academic Press, Burlington MA, 2009.
- [3] H.C. Schau and A.Z. Robinson, “Passive Sources Localization Employing Intersecting Spherical Surfaces from Time-of-Arrival Differences”, IEEE Transactions on Acoustics, Speech, and Signal Processing, Vol. ASSP-35, No. 8, pp. 1223–1225, August 1987.
- [4] J. Abel and J. Chaffe, “Existence and Uniqueness of GPS Solutions”, IEEE Transactions on Aerospace and Electronic Systems, Vol. 27, No. 6, pp. 952–956, November 1991.
- [5] J. Bard, F.M. Ham, and W.L. Jones, “An Algebraic Solution to the Time-Difference of Arrival Equations”, Southeastcon ’96, Proceedings of the IEEE, pp. 313–319, Tampa, FL, 11–14 April 1996.
- [6] T. Sathyan, A. Sinha, and T. Kirubarajan, “Passive Geolocation and Tracking of an Unknown Number of Emitters”, IEEE Transactions on Aerospace and Electronic Systems, Vol. 42, No. 2, pp. 740–750, April 2006.
- [7] M. Wax and T. Kailath, “Optimum Localization of Multiple Sources by Passive Arrays”, IEEE Transactions on Acoustics, Speech, and Signal Processing, Vol. ASSP-31, No. 5 pp. 1210–1217, October 1983.
- [8] Y.T. Chan and K.C. Ho, “A Simple and Efficient Estimator for Hyperbolic Location”, IEEE Transactions on Signal Processing, Vol. 42, No. 8, pp. 1905–1915, August 1994.
- [9] G. Mellen, M. Pachter, and J. Raquet, “Closed-Form Solution for Determining Emitter Location using Time Difference of Arrival Measurements”, IEEE Transactions on Aerospace and Electronic Systems, Vol. 39, No. 3, pp. 1056–1058, July 2003.
- [10] B. Fang, “Simple Solution for Hyperbolic and Related Position Fixes”, IEEE Transactions on Aerospace and Electronic Systems, Vol. 26, No. 5, pp. 748–753, September 1990.
- [11] F.C. Schweppe, “Sensor Array Data Processing for Multiple Signal Sources”, IEEE Transactions on Information Theory, Vol. IT-14, pp. 294–305, February 1968.
- [12] R. Schmidt, “Least Squares Range Difference Location”, IEEE Transactions on Aerospace and Electronic Systems, Vol. 32, No. 1, pp. 234–242, January 1996.
- [13] J.P. Van Etten, “Navigation Systems: Fundamentals of Low- and Very-Low-Frequency Hyperbolic Techniques”, Electrical Communication, Vol. 45, No. 3, pp. 192–212, 1970.

- [14] R.O. Schmidt, "A New Approach to Geometry of Range Difference Location", IEEE Transactions on Aerospace and Electronic Systems, Vol. AES-8, No. 6, pp. 821–835, November 1972.
- [15] D.A. Brannan, M.F. Esplen, and J. J. Grey, "Geometry", Cambridge University Press, 1999.
- [16] J.O. Smith and J.S. Abel, "Closed-Form Least-Square Source Location Estimation from Range-Difference Measurements", IEEE Transactions on Acoustics, Speech, and Signal Processing, Vol. ASSP-35, No. 12, pp. 1661–1669, December 1987.
- [17] W.H. Foy, "Position Location Solution by Taylor Series Estimation", IEEE Transactions on Aerospace and Electronic Systems, Vol. AES-12, pp. 183–198, March 1976.
- [18] D.J. Torrieri, "Statistical Theory of Passive Location Systems", IEEE Transactions on Aerospace and Electronic Systems, Vol. AES-20, No. 2, pp. 183–197, March 1984.
- [19] H.C. So, Y.T. Chan, and F. Chan, "Closed-Form Formulae for Time-Difference-Of-Arrival Estimation", IEEE Transactions on Signal Processing, Vol. 56, No. 6, pp. 2614–2620, June 2008.
- [20] M. Khalaf-Allah, "A Modified Closed-Form Time-Difference-Of-Arrival Positioning Algorithm", Proc. Of World Symposium on Computer Network and Information Security, <http://nngt.org/digital-library/upload/conference2/p2.pdf> (Access date: March 2016).
- [21] W.R. Hahn and S.A. Tretter, "Optimum Processing for Delay-Vector Estimation in Passive Signal Arrays", IEEE Transactions on Information Theory, Vol. IT-19, No. 5, pp. 608–614, September 1973.
- [22] S. Stein, "Algorithms for Ambiguity Function Processing", IEEE Transactions on Acoustics, Speech, and Signal Processing, Vol. ASSP-29, No. 3, pp. 588–599, June 1981.
- [23] C.H. Knapp and G.C. Carter, "The Generalized Correlation Method for Estimation of Time Delay", IEEE Transactions on Acoustics, Speech, and Signal Processing, Vol. ASSP-24, No. 4, pp. 320–327, August 1976.
- [24] R.N. McDonough and A.D. Whalen, "Detection of Signal in Noise", Second Edition, Academic Press, 1995.
- [25] A.H. Quazi, "An Overview on the Time Delay Estimation in Active and Passive Systems for Target Localization", IEEE Transactions on Acoustics, Speech, and Signal Processing, Vol. ASSP-29, No. 3 pp. 527–533, June 1981.
- [26] A.W. Rihaczek, "Principles of High Resolution Radar", Artech House, Boston, 1996.
- [27] R.S. Berkowitz, "Modern Radar: Analysis, Evaluation and System Design", John Wiley & Sons, Inc., New York, 1965.
- [28] "Radar Handbook", Editor, M. Skolnik, Second Edition, McGraw-Hill, 1990.

- [29] D.R. Wehner, “High Resolution Radar”, Artech House, Boston, 1987.
- [30] “Coherent Radar Performance Estimation”, Editors, J.A. Scheer and J.L. Kurtz, Artech House, Boston, 1993.
- [31] S.K. Wong, “High Range Resolution Profiles as Motion-Invariant Features for Moving Ground Target Identification in SAR-based Automatic Target Recognition”, IEEE Transactions on Aerospace and Electronic Systems, Vol. 45, No. 3, pp. 1017–1039, July 2009.
- [32] S. Henriksen, “Unmanned Aircraft Control and ATC Communications Bandwidth Requirements”, NASA/CR-2008-214841, 2008.
- [33] R.J. Sullivan, “Radar Foundations for Imaging and Advanced Concepts”, SciTech Publishing, NC, 2004.
- [34] “Digital TV: A Cringley Crash Course – Digital Vs. Analog”,
http://isites.harvard.edu/fs/docs/icb.topic86897.files/September_20/PBS_digital_TV.pdf
 (Access date: October 2015).
- [35] <https://www.firstpersonview.co.uk/transmission/5.8GHz> (Access date: October 2015).
- [36] H. Cantalloube and P. Dubois-Fernandez, Airborne, X-band SAR imaging with 10 cm resolution: technical challenge and preliminary results, IEE Proc.-Radar Sonar Navig., Vol. 153, No. 2, pp.163–176, April 2006,
<http://ieeexplore.ieee.org/stamp/stamp.jsp?arnumber=1626085> (Access date: 17 February 2017).

This page intentionally left blank.

Annex A Frequency waveforms

Different radar systems employ different radar waveforms, depending on the system hardware and the applications. There are, in general, three major classes of radar waveforms deployed in operational imaging radar systems: stepped-frequency waveform (SFWF), pulse-compression waveform (PCWF) and frequency-modulation continuous waveform (FMCW). In radar image processing, detected signals from a target, regardless of the waveforms used by the radar systems, are first demodulated into baseband signals in the form of in-phase (I) and quadrature (Q) signals in the frequency domain. The (I,Q) signals are then processed into SAR images. The (I,Q) signal is commonly given by the stepped-frequency format; this representation is compatible with all three radar waveforms mentioned above. A common (I,Q) format allows a conceptually universal procedure for processing SAR images, although there are some practical details to be sorted out, for example, pulse repetition rate, pulse bandwidth and pulse duration, to differentiate the different waveforms. A description on how a common (I,Q) format, using the stepped-frequency representation, can represent all three radar waveforms and how the (I,Q) signals are used in processing SAR images is given in this section.

The stepped-frequency radar waveform is composed of a series of short radar pulses. Each pulse may be 200 ns to 1 μ s in duration; thus the transform limited bandwidth of each short pulse is only 1 to 5 MHz wide in instantaneous bandwidth. To compose a waveform with a much larger effective bandwidth (i.e., hundreds of MHz), a sequence of these short pulses is employed where the carrier frequency of each pulse is increased by an amount Δf between successive pulses,

$$f_n = f_0 + n\Delta f \quad (\text{A.1})$$

where the subscript n is the incrementing index, $n = 0, 1, \dots, N-1$ and the effective bandwidth $\beta = (N-1)\Delta f$. Since the frequency is increased by an amount Δf at every time increment, Δt between successive pulses, the temporal phase history of the SFWF can be expressed as,

$$\begin{aligned} \varphi(t) &= 2\pi f(t)t \\ &= 2\pi(f_0 + n\Delta f)(t_0 + n\Delta t) \\ &= 2\pi[f_0 t_0 + n(\Delta f t_0 + f_0 \Delta t) + n^2(\Delta f \Delta t)] \\ &= k_0 + k_1 n + k_2 n^2 \end{aligned} \quad (\text{A.2})$$

where $k_0, k_1, k_2, f_0, t_0, \Delta f$ and Δt are constants. It should note that the incrementing index n , acts as a “time” variable. An illustration of the stepped frequency waveform is given in Figure A.1. The corresponding (I,Q) data in the frequency domain from a sequence of stepped-frequency radar pulses are given by,

$$(I, Q)_n = A_n \exp \left[j \frac{4\pi f_n}{c} R(t) \right] \quad (\text{A.3})$$

where A_n is the amplitude of the received signal at frequency f_n as given by Equation (A.1), and $R(t)$ is given by Equation (31).

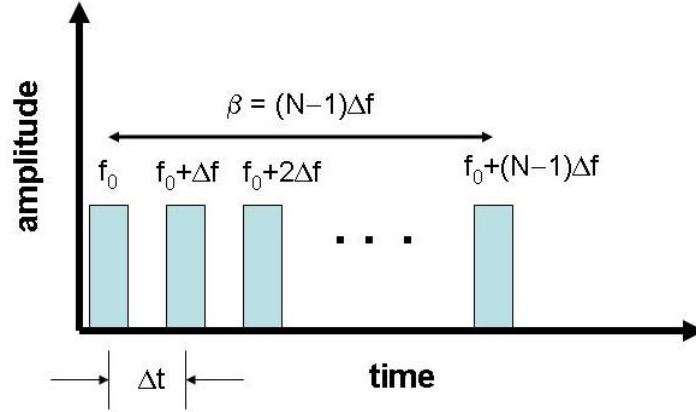


Figure A.1: Schematic of the stepped-frequency waveform.

The pulse-compression waveform is a single radar pulse that contains a wide frequency band. The wide bandwidth is obtained by chirping the carrier frequency band over the duration of the radar pulse. A schematic of the pulse-compression waveform is shown in Figure A.2. The frequency chirping is given by,

$$f(t) = f_0 + mt \quad (\text{A.4})$$

where m is the frequency chirp rate (i.e., the slope in the frequency versus time plot in Figure A.2). The phase of the PCWF is given by,

$$\begin{aligned} \varphi(t) &= 2\pi f(t)t \\ &= \varphi_0 + 2\pi f_0 t + 2\pi \frac{m}{2} t^2 \\ &= c_0 + c_1 t + c_2 t^2 \end{aligned} \quad (\text{A.5})$$

such that the instantaneous frequency is

$$\begin{aligned}
f(t) &= \frac{1}{2\pi} \frac{d\varphi}{dt} \\
&= f_0 + mt
\end{aligned}
\tag{A.6}$$

From Figure A.2, it is seen that the frequency chirp rate can be determined as,

$$m = \frac{f_e - f_0}{t_e - t_0} = \frac{\beta}{T} \tag{A.7}$$

where β is the frequency bandwidth and T is the duration of the chirp. A more accurate expression for the frequency chirp rate, m is given by

$$m = \frac{2\beta_e}{T} \tag{A.8}$$

where β_e is an effective bandwidth. A vigorous derivation of the chirping rate m can be found in [27]. The important thing to note here is that the temporal behaviour of the phase φ in Equation (A.5) for PCFW has exactly the same form as the SFWF given by Equation (A.2). And the frequency increase due to chirping in Equation (A.4) is identical to the frequency increase in the stepped-frequency case as given by Equation (A.1). Thus accordingly, the (I,Q) signal format for the PCWF can also be represented by the Equation (A.3).

Similarly, the frequency-modulated continuous waveform (FMCW) as depicted in Figure A.3 can be shown to have the same temporal characteristics as the PCWF; i.e., the frequency chirping and the phase of the FMCW waveform can also be described by Equations (A.4) and (A.5) respectively. Detailed analysis of the FMCW waveform can be found in [27]. Consequently, the (I,Q) signal for the FMCW waveform can also be represented by Equation (A.3).

To summarize, the common temporal phase characteristics of the three different radar waveforms imply that the in-phase and quadrature signals can be formatted using a common framework. This justifies the use of the stepped-frequency format in representing the (I,Q) data.

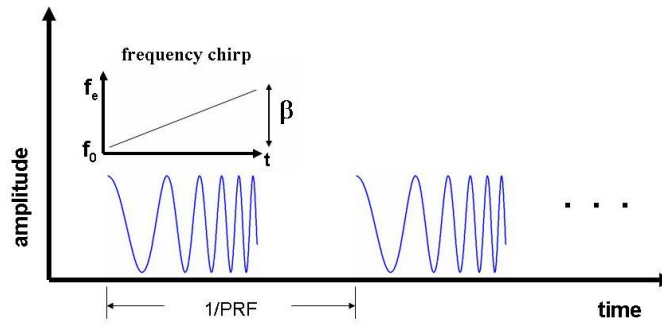


Figure A.2: Schematic of the chirp pulse-compression waveform.

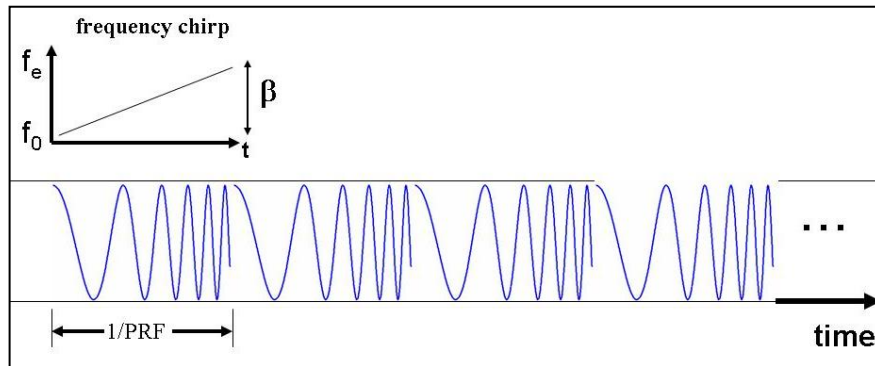


Figure A.3: Schematic of the frequency-modulated continuous waveform.

List of symbols/abbreviations/acronyms/initialisms

CAF	Canadian Armed Forces
CRLB	Cramer-Rao Lower Bound
EIRP	Effective Isotropic Radiated Power
FDOA	Frequency-Difference-of-Arrival
ISR	Intelligence, Surveillance and Reconnaissance
LORAN	Long Range Navigation
LOS	Line-of-Sight
RF	Radio-Frequency
SAR	Synthetic Aperture Radar
SNR	Signal-to-Noise Ratio
TDOA	Time-Difference-of-Arrival

This page intentionally left blank.

DOCUMENT CONTROL DATA		
(Security markings for the title, abstract and indexing annotation must be entered when the document is Classified or Designated)		
1. ORIGINATOR (The name and address of the organization preparing the document. Organizations for whom the document was prepared, e.g., Centre sponsoring a contractor's report, or tasking agency, are entered in Section 8.) DRDC – Ottawa Research Centre Defence Research and Development Canada 3701 Carling Avenue Ottawa, Ontario K1A 0Z4 Canada		2a. SECURITY MARKING (Overall security marking of the document including special supplemental markings if applicable.) UNCLASSIFIED
		2b. CONTROLLED GOODS (NON-CONTROLLED GOODS) DMC A REVIEW: GCEC DECEMBER 2013
3. TITLE (The complete document title as indicated on the title page. Its classification should be indicated by the appropriate abbreviation (S, C or U) in parentheses after the title.) Passive target localization using a geometric approach to the time-difference-of-arrival method		
4. AUTHORS (last name, followed by initials – ranks, titles, etc., not to be used) Wong, S.; Jassemi-Zargani, R.; Brookes, D.; Kim, B.		
5. DATE OF PUBLICATION (Month and year of publication of document.) June 2017	6a. NO. OF PAGES (Total containing information, including Annexes, Appendices, etc.) 77	6b. NO. OF REFS (Total cited in document.) 36
7. DESCRIPTIVE NOTES (The category of the document, e.g., technical report, technical note or memorandum. If appropriate, enter the type of report, e.g., interim, progress, summary, annual or final. Give the inclusive dates when a specific reporting period is covered.) Scientific Report		
8. SPONSORING ACTIVITY (The name of the department project office or laboratory sponsoring the research and development – include address.) DRDC – Ottawa Research Centre Defence Research and Development Canada 3701 Carling Avenue Ottawa, Ontario K1A 0Z4 Canada		
9a. PROJECT OR GRANT NO. (If appropriate, the applicable research and development project or grant number under which the document was written. Please specify whether project or grant.)	9b. CONTRACT NO. (If appropriate, the applicable number under which the document was written.)	
10a. ORIGINATOR'S DOCUMENT NUMBER (The official document number by which the document is identified by the originating activity. This number must be unique to this document.) DRDC-RDDC-2017-R079	10b. OTHER DOCUMENT NO(s). (Any other numbers which may be assigned this document either by the originator or by the sponsor.)	
11. DOCUMENT AVAILABILITY (Any limitations on further dissemination of the document, other than those imposed by security classification.) Unlimited		
12. DOCUMENT ANNOUNCEMENT (Any limitation to the bibliographic announcement of this document. This will normally correspond to the Document Availability (11). However, where further distribution (beyond the audience specified in (11) is possible, a wider announcement audience may be selected.) Unlimited		

13. **ABSTRACT** (A brief and factual summary of the document. It may also appear elsewhere in the body of the document itself. It is highly desirable that the abstract of classified documents be unclassified. Each paragraph of the abstract shall begin with an indication of the security classification of the information in the paragraph (unless the document itself is unclassified) represented as (S), (C), (R), or (U). It is not necessary to include here abstracts in both official languages unless the text is bilingual.)

Passive sensing offers a viable and effective means of detecting and geolocating small flying targets such as micro- and nano-drones by exploiting their radio-frequency signal emissions. Target location using the time-difference-of-arrival (TDOA) method is investigated. For target localization in three-dimensional space, a set of three non-linear TDOA equations is required. Each equation contains a TDOA measurement processed from signals detected by a pair of receivers. A system of four receivers is needed to generate three independent TDOA measurements. The solution to each TDOA equation is represented by a hyperboloid surface. The intersection of three hyperboloid surfaces is then computed to determine the target location. This geometric approach to solving the TDOA problem is taken in this study.

The target localization problem is analyzed by examining the effect of TDOA measurement errors on the localization accuracy. The errors are modelled by the Cramer-Rao Lower Bound estimate in processing the signals through a cross-correlator. Results indicate that the accuracy in three-dimensional target localization is dependent on not only the TDOA measurement errors, but also on the receiver system geometry. It is found that four receivers in a non-coplanar geometry configuration offer the best three-dimensional localization accuracy.

Localization of multiple targets is also investigated. Accurate localization results for up to ten moving targets have been obtained by applying the geometric approach. A discussion on how the geometric approach could be exploited for real-time multi-target localization is given. This will potentially offer a practical capability in defence and security applications.

Le captage passif offre un moyen viable et efficace de détecter et de géolocaliser de petites cibles volantes, par exemple des microdrones et des nanodrones, en exploitant leurs émissions de signaux en radiofréquence. La détermination de l'emplacement de la cible grâce à la méthode de la différence entre les temps d'arrivée (TDOA) est à l'étude. Pour localiser la cible dans un espace tridimensionnel, un ensemble de trois équations TDOA non linéaires est nécessaire. Chaque équation contient une mesure de TDOA traitée à partir des signaux détectés par une paire de récepteurs. Un système à quatre récepteurs est nécessaire pour générer trois mesures de TDOA indépendantes. La solution à chaque équation de TDOA est représentée par une surface hyperboloïde. L'intersection de trois surfaces hyperboloïdes est ensuite calculée afin de déterminer l'emplacement de la cible. C'est cette méthode géométrique qui est utilisée pour résoudre le problème de TDOA dans l'étude en question.

Le problème de repérage d'une cible est analysé en examinant l'effet des erreurs de mesure de TDOA sur l'exactitude du repérage. Les erreurs sont modélisées par l'estimation de la borne inférieure de Cramer-Rao pour le traitement des signaux par l'entremise d'un récepteur à corrélateur croisé. Les résultats indiquent que l'exactitude du repérage tridimensionnel d'une cible dépend non seulement des erreurs de mesure de TDOA, mais aussi de la géométrie du système de récepteur. On a déterminé qu'une configuration à quatre récepteurs disposés selon une géométrie non-coplanaire offrait la plus grande exactitude de repérage tridimensionnel.

Le repérage de cibles multiples est aussi à l'étude. Des résultats de repérage exacts pour jusqu'à

dix cibles en mouvement ont été obtenus en appliquant la méthode géométrique. Un exposé est donné sur la façon dont la méthode géométrique pourrait être exploitée pour repérer des cibles multiples en temps réel. Cette méthode a le potentiel d'offrir des applications pratiques pour la défense et la sécurité.

14. **KEYWORDS, DESCRIPTORS or IDENTIFIERS** (Technically meaningful terms or short phrases that characterize a document and could be helpful in cataloguing the document. They should be selected so that no security classification is required. Identifiers, such as equipment model designation, trade name, military project code name, geographic location may also be included. If possible keywords should be selected from a published thesaurus, e.g., Thesaurus of Engineering and Scientific Terms (TEST) and that thesaurus identified. If it is not possible to select indexing terms which are Unclassified, the classification of each should be indicated as with the title.)

passive detection; cross-correlation; signal processing; time difference of arrival; target localization; multiple targets; counter-measures; drone surveillance